

# The Tilted-Ellipse Representation of Standing-Wave Patterns.

*Ross A. Speciale*  
*Research & Development Inc.*  
*email: [rspeciale@comcast.net](mailto:rspeciale@comcast.net)*

## *Abstract.*

A recently introduced, new computer-simulation method provides a fast and inexpensive way for obtaining the multi-dimensional scattering matrices of even very large-scale, multiport microwave systems. The new method simulates measurements of multidimensional, complex scattering matrices, that could only be performed using a very large and expensive multiport Vector Network Analyzer (VANA). Calibrated measurements of complex scattering matrices of any arbitrary size may be simulated by using any available frequency-domain 2D or 3D Maxwell-field solver, provided the solver used can compute the *complex values* of EM fields, within a given bounded domain. Scattering-matrix measurements, that would require an impractically-large and expensive multiport Vector Network Analyzer (VANA), can be simulated by first computing the electromagnetic field-distributions, within both the multiport microwave system under simulated test (the *virtual* DUT or V-DUT), and within the inner regions of a set of simulated *virtual measurement-lines* (V-ML), with each line being connected to a different V-DUT port.

The simulation of multidimensional, complex scattering-matrix measurements is based on the results of a rigorous mathematical analysis of the simultaneous propagation of forward and backward waves along the virtual measurement lines. This rigorous analysis has shown that the mutual correlation between the imaginary components, and the real components of the standing-wave fields, along the length of each measurement-line, can be quantitatively represented by the parametric equations of a tilted-ellipse, centered on the origin of a 2D planar, Cartesian reference-frame.

## **1. Objective.**

This paper shows how the geometric parameters, of the tilted-ellipse representation of the standing-wave pattern along each virtual line, may be used to compute the magnitudes and the phases of the forward-wave and backward-wave vectors, at any arbitrary point along each of the virtual measurement-lines that is simulated as being connected to one of the various V-DUT ports. In this tilted-ellipse representation, the imaginary components  $V_I$  of the standing-wave fields, computed by the solver along the  $z$ -axes of the simulated measurement lines, are displayed along the ordinate-axis  $\zeta$  of a 2D  $(\xi, \zeta)$  planar-Cartesian reference-frame, while the corresponding real components  $V_R$  are displayed along the reference-frame abscissa-axis  $\xi$ .

The mathematical results of the previously reported rigorous analysis of the simultaneous propagation of the forward and backward waves [1], express the complex values of the forward-wave vectors  $V_F(z)$ , and backward-wave vectors  $V_B(z)$ , as functions of the distance  $z$  from each V-DUT system port.

Those rigorous expressions provide a new way of extracting the complex values of both the forward-wave and the backward-wave vectors, from the standing-wave field-patterns computed by the EM solver used, along each of the virtual measurement-lines.

Report Documentation Page				Form Approved OMB No. 0704-0188	
Public reporting burden for the collection of information is estimated to average 1 hour per response, including the time for reviewing instructions, searching existing data sources, gathering and maintaining the data needed, and completing and reviewing the collection of information. Send comments regarding this burden estimate or any other aspect of this collection of information, including suggestions for reducing this burden, to Washington Headquarters Services, Directorate for Information Operations and Reports, 1215 Jefferson Davis Highway, Suite 1204, Arlington VA 22202-4302. Respondents should be aware that notwithstanding any other provision of law, no person shall be subject to a penalty for failing to comply with a collection of information if it does not display a currently valid OMB control number.					
1. REPORT DATE <b>24 FEB 2004</b>		2. REPORT TYPE <b>N/A</b>		3. DATES COVERED <b>-</b>	
4. TITLE AND SUBTITLE <b>The Tilted-Ellipse Representation of Standing-Wave Patterns</b>				5a. CONTRACT NUMBER	
				5b. GRANT NUMBER	
				5c. PROGRAM ELEMENT NUMBER	
6. AUTHOR(S)				5d. PROJECT NUMBER	
				5e. TASK NUMBER	
				5f. WORK UNIT NUMBER	
7. PERFORMING ORGANIZATION NAME(S) AND ADDRESS(ES) <b>Research &amp; Development Inc.</b>				8. PERFORMING ORGANIZATION REPORT NUMBER	
9. SPONSORING/MONITORING AGENCY NAME(S) AND ADDRESS(ES)				10. SPONSOR/MONITOR'S ACRONYM(S)	
				11. SPONSOR/MONITOR'S REPORT NUMBER(S)	
12. DISTRIBUTION/AVAILABILITY STATEMENT <b>Approved for public release, distribution unlimited</b>					
13. SUPPLEMENTARY NOTES <b>See also ADM001763, Annual Review of Progress in Applied Computational Electromagnetics (20th) Held in Syracuse, NY on 19-23 April 2004., The original document contains color images.</b>					
14. ABSTRACT					
15. SUBJECT TERMS					
16. SECURITY CLASSIFICATION OF:			17. LIMITATION OF ABSTRACT <b>UU</b>	18. NUMBER OF PAGES <b>53</b>	19a. NAME OF RESPONSIBLE PERSON
a. REPORT <b>unclassified</b>	b. ABSTRACT <b>unclassified</b>	c. THIS PAGE <b>unclassified</b>			

The new scattering-matrix measurement-simulation method performs therefore the very same wave-extraction function that, in an actual experimental measurement session, would require the use of a Vector-Reflectometer, composed of two appropriately-oriented Directional Couplers and of a Vector-Voltmeter.

The complex values of the forward-wave and backward-wave vectors so extracted may then be mutually correlated, by computing complex wave-correlation ratios  $\Gamma(\mathbf{z})$  between each forward-wave vector  $\mathbf{V}_F(\mathbf{z})$  and the corresponding backward-wave vector  $\mathbf{V}_B(\mathbf{z})$ , when those two vectors propagate on the same virtual measurement-line line. Similarly, line-to-line wave-correlation ratios  $\Gamma_{ij}(\mathbf{z})$  may be computed as the ratios of a backward-wave vector  $\mathbf{V}_{Bi}(\mathbf{z})$ , that propagates on virtual measurement-line line  $i$ , to a forward-wave vector  $\mathbf{V}_{Fj}(\mathbf{z})$ , that propagates on a different virtual measurement-line line  $j$ .

The complex wave-correlation ratios between a backward-wave vector and a forward-wave vector are defined as  $\Gamma_{ij}(\mathbf{z}) = \mathbf{V}_{Bj}(\mathbf{z}) / \mathbf{V}_{Fi}(\mathbf{z})$ , and represent at the location  $\mathbf{z} = 0$  of each V-DUT port, either the value of a diagonal scattering-matrix element  $\mathbf{S}_{ii}$  (for  $i = j$ ), or the value of an off-diagonal scattering-matrix element  $\mathbf{S}_{ij}$  (for  $i \neq j$ ).

Most remarkably, the complex vectors  $\mathbf{V}_{Fi}(\mathbf{z})$ , and  $\mathbf{V}_{Bj}(\mathbf{z})$ , and the mutual complex correlation-ratios  $\Gamma_{ij}(\mathbf{z})$ , that clearly characterize the simultaneous propagation of the measurement signals, along a set of  $n$  measurement-lines, can be expressed at any given distance  $\mathbf{z}$  from one of the V-DUT system port (assumed located at  $\mathbf{z} = 0$ ), as functions of the geometric parameters  $\mathbf{a}_i$ ,  $\mathbf{b}_i$ , and  $\delta_i$  ( $i = 1, 2, \dots, n$ ) of the tilted-ellipse representations of the standing-wave patterns along each of the  $n$  virtual measurement lines, and of the polar angle  $\Phi_{\xi\zeta}(\mathbf{z}) = \arctan(\zeta / \xi)$  of the tilted-ellipse radius-vector (Figure 2).

The geometric parameter  $\mathbf{a}_i$  of each tilted-ellipse measures the length of its major semi-axis, while the geometric parameter  $\mathbf{b}_i$  measures the length of its minor semi-axis. Similarly, the angular parameter  $\delta_i$  measures the tilt-angle of each ellipse major axis, relative to the abscissa-axis  $\xi$  of the 2D  $(\xi, \zeta)$  planar-Cartesian reference-frame used. The geometric distance  $\mathbf{z}$  is assumed to be increasing on each virtual line in positive value, from the  $\mathbf{z} = 0$  line-end connected to one of the multiport-system ports, towards the line-end connected to either the measurement signal-source, or to an auxiliary load.

## 2. Advantages of Measurement- Simulations.

Clearly, very significant time and cost savings may be attained by simulating S-matrix experimental measurements, when the system under simulated test has a very large number of ports ( $n > 4$ ), and possibly also a very large number of different propagating modes. In such cases, the design and hardware-integration of a physical Multiport Vector Network Analyzer, and the execution of the required numerous, and labor-intensive data-acquisitions, would be prohibitively expensive and highly impractical. Quite to the contrary, the measurement-simulation method described here makes now possible to even consider (*as just a representative example*) the simulation of the multidimensional-scattering-matrix measurements required to evaluate the radiation-pattern of a dual-polarization, electronically-steered phased array, set-up in view of a near-field scanning system (Figure 1). Indeed, using the here described new method, such simulation would even be practically feasible, if the array were to be simulated as having *no beam-forming network*, but being rather directly excited, by connecting each of its many elements to a different input virtual-line.

### 3. Simulation of the Measurement Lines.

The virtual measurement-lines, that are simulated as being connected to the various ports of the multiport microwave system under test (the V-DUT), must be assumed to be *lossless* and *uniform*, to assure that both the forward-waves and the backward waves propagate with unattenuated constant-amplitude, and linear phase-evolution along the length of each line. Further, the physical configurations of each virtual transmission line, and the shape and size of its cross-section must be quantitatively defined, to be precisely consistent with the geometry of the corresponding V-DUT system port. The physical type of each measurement-line, and the shape and size of its cross-section need not be identical to that of any other line, but may rather be arbitrarily different, as required to be consistent with the geometry of the corresponding system port. Further, the physical layout and geometry of the signal-coupling means of the measurement-signal source to the corresponding line must be selectively simulated for different lines, so that the wave-mode of both the forward-wave and the backward wave be the one specifically required for the excitation of the corresponding V-DUT port.

Also, either the frequency of the measurement-signal must be set higher than the cut-off of the selected fundamental mode, and lower than the cut-off of the next-higher mode, or a mode-filter must be introduced at the output of the signal-source, if the wave-mode required by the simulated measurement is not the fundamental mode of the specific measurement-line.

The simulation of different measurement-line types, propagating different wave-modes automatically makes the multidimensional scattering matrix obtained a *Generalized Scattering Matrix*, that is normalized at each port of the V-DUT to the wave-impedance value of the specifically-selected common wave-mode of both the line forward-wave and the line backward-wave.

Finally, an impedance-matched attenuator must be simulated as being inserted between the signal-source and the virtual measurement-line, to introduce an attenuation in the order of 30 - 40 dB immediately at the line input. This expedient prevents any simultaneous impedance-mismatch affecting both ends of a measurement-line from creating a double-reflection pattern between the two line ends. As generally known, such double-reflections create a frequency-selective, *resonant* standing-wave pattern along the affected measurement line. A line-input attenuator may easily be simulated in the form of a short slab of lossy dielectric material, having the ratio of its complex relative-permeability  $\mu_R$  to its complex relative permittivity  $\epsilon_R$  equal to the square of the line wave-impedance. Such slab of dielectric material, with complex relative-permeability  $\mu_R = \mu_R' + j \mu_R''$  and complex relative-permittivity  $\epsilon_R = \epsilon_R' + j \epsilon_R''$  must be inserted orthogonally to the line axis, immediately at its input port.

### 4. Least-Squares-Fitting of the Ellipses.

The Cartesian coordinates  $\xi$ ,  $\zeta$  of each tilted-ellipse representation of a standing-wave pattern respectively display the real, and the imaginary components of the electromagnetic field, as computed by the Maxwell solver used within the inner region of the corresponding virtual measurement-line. The complex values of the standing-wave pattern along each line are however only available on the nodes of the 2D or 3D mesh used by the solver to discretize the domain of the solution. Clearly the mesh nodes are however not necessarily aligned along the axis of the line, and further even the complex field-values computed by the solver on the mesh-nodes are known to be only approximate. Fortunately, the previously reported rigorous analysis [1] provides the fundamental *a-priori knowledge* of the fact that the correlation between the real and imaginary field-components can be exactly represented by the parametric equations of a *perfect tilted-ellipse*. This fundamental result provides a powerful capability for very substantially reducing the adverse effects of both the mesh discretization, and the finite accuracy of the computed field solutions.

Indeed, theoretically-unlimited accuracy-enhancements may be attained by performing a 2D Least-Squares fitting of the tilted-ellipse  $\xi$  and  $\zeta$  coordinates to the computed field-values, using the parametric equations of a perfect tilted-ellipse, and by progressively increasing the number of input field-values.

## 5. Iterative Accuracy Enhancement.

The magnitude of the accuracy enhancement, obtained by using any suitable tilted-ellipse Least-Squares-Fitting algorithm, becomes obviously increasingly larger if increasingly larger numbers of computed field values are collected and used as the algorithm input-data. The attained accuracy of the result may then be measured by computing the residual least-squares error [1], that globally expresses the *distance* of the computed best-fit ellipse from the set of field values used as input data. This possibility of progressively enhancing the accuracy of the tilted-ellipse fit in terms of its geometric parameters, suggests the convenience of using an iterative procedure, that cyclically increases the number of EM field-values used as input data, and compares at every step of the iteration the last values of the residual least-squares error, and the last values of the ellipse geometric parameters, to the corresponding values obtained from the previous iteration cycle. Clearly, a criterion may be defined for terminating the iteration process, when either the residual least-squares error does no-longer substantially decrease, or the geometric parameters of the best-fit tilted-ellipse obtained no-longer substantially change.

## 6. Evaluation of Relative Solver-Accuracy.

Most remarkably, the size of the best-fit tilted-ellipse residual least-squares error clearly provides a measure of the accuracy of the Maxwell solver used. The relative accuracy of different Maxwell solvers may then be evaluated, by running identical simulations of the same multiport microwave system using different solvers, and by comparing the progressive evolutions of the residual least-squares errors, and of the tilted-ellipse geometric parameters, obtained by using identical numbers of EM input field-values, at every step of identical cyclic-iteration procedures.

A tilted-ellipse Least-Squares-Fitting algorithm has already been developed, specifically for this application, and was already described in [1]. That previously-developed Least-Squares-Fitting algorithm described in [1] is however specifically intended for fitting a tilted-ellipse to a given set of field-values, with the restriction that the resulting ellipse be *centered* on the origin of the  $(\xi, \zeta)$  Cartesian reference-frame.

Any other Least-Squares-Fitting algorithm may however be used, and in particular any of the algorithms that fit a tilted-ellipse centered at *any arbitrary point* of the  $(\xi, \zeta)$  Cartesian plane. All such algorithms are notoriously more computationally-intensive, due to the requirement of computing, besides the lengths of the two semi-axes  $\mathbf{a}$  and  $\mathbf{b}$ , and of the tilt-angle  $\delta$ , also the Cartesian coordinates  $\xi$  and  $\zeta$  of the ellipse center.

The use of such Least-Squares-Fitting algorithm, in the comparative evaluation of the relative accuracy of different solvers, may however reveal the existence in either or both field-solutions of possible *bias errors*. Such errors would be evidenced by a shift of the ellipse center from the origin, and would be measured by the length of the ellipse-center shift, resulting from using equal-sized sets of input field-values computed by using different alternative solvers.

## 7. From Geometric Parameters to Electromagnetic Vectors.

Each of the  $n$  tilted ellipses that represent the standing-wave patterns along the various simulated measurement-lines is characterized by its three geometric parameters: a) the major semi-axis  $a$ , b) the minor semi-axis  $b$ , and c) the tilt-angle  $\delta$ .

Five other geometric parameters must also be considered in each of the tilted-ellipse representations: 1. the Cartesian coordinates  $x(z)$  and  $y(z)$  of the ellipse points, displayed along the ellipse major and minor axes; 2. the polar angle  $\phi_{\xi\zeta}(z)$  relative to the rotated Cartesian axes  $\xi$  and  $\zeta$ ; 3. the polar angle  $\phi_{xy}(z)$  relative to the non-rotated Cartesian axes  $x$  and  $y$ ; and 4. the independent angular-parameter  $\theta(z)$  used in the two parametric equations of a non-tilted ellipse, in the  $x, y$  reference-frame. Those eight geometric parameters are all clearly identified in Figure 2, that also shows the most well-known and classic graphic construction of a centered, non-tilted ellipse displayed on the  $x, y$  axis-system.

The computation of the elements of the multi-dimensional scattering matrix of a multiport system under simulated test (the V-DUT) requires that those eight geometric parameters of each ellipse be correlated to the complex values of the forward-wave vector  $V_{Fi}(z)$ , of the backward-wave vector  $V_{Bi}(z)$ , and of the corresponding wave-correlation-ratio  $\Gamma_{ij}(z)$ . Clearly, the eight geometric parameters and the three complex electrical vectors are all functions of the geometric distance  $z$ , measured along the axis of each virtual line, starting from the locations  $z = 0$  of its V-DUT port. Further, the *electrical distance* from that V-DUT port, expressed by  $\psi(z) = 2\pi z / \lambda$ , must also be considered, as it determines the *linear* evolutions of the *phase-angles* of the forward-wave vector  $V_{Fi}(z)$ , of the backward-wave vector  $V_{Bi}(z)$ , and of the mutual wave-correlation-ratio  $\Gamma_{ii}(z)$ .

A mutual correspondence must obviously be established between the points  $(\xi, \zeta)$  around each tilted-ellipse, and the geometric distance  $z$  from the V-DUT port, along the corresponding virtual measurement-line. The  $m$  field-values of the standing-wave pattern, used as Least-Squares-Algorithm inputs, must correspond to known values  $z_i$  of the  $z$ -coordinate, along each measurement-line, and those  $z$ -coordinate values must be associated with the points  $(\xi, \zeta)$  of the tilted-ellipse that are *closest* to the points  $(\xi_i, \zeta_i)$  that represent the  $m$  field-values, used as inputs for the Least-Squares Algorithm.

Those tilted-ellipse points are defined as the intersections of the ellipse with the straight line, orthogonal to the  $x$ -axis, that runs through the points  $(\xi_i, \zeta_i)$  that represents each of the input field-values. The distance  $r$  between the points  $(\xi_i, \zeta_i)$  and  $(\xi, \zeta)$  obviously measures the local deviation  $\mathcal{E}_i$ , of each point  $(\xi_i, \zeta_i)$ , from the tilted-ellipse, at the intersection with the local normal to the  $x$ -axis (Figure 5).

The use of input field-values represented by points  $(\xi_i, \zeta_i)$ , obtained at equally-spaced points  $z_i$  along the  $z$ -coordinate of each given measurement line, is quite clearly very advantageous, as such points imply a linear dependence of the local values of the phase-angles of both the forward-wave and backward-wave vectors  $V_{Fi}(z_i)$ , and  $V_{Bi}(z_i)$ , as functions of the geometric-distance  $z$ -coordinate.

### 8. Parametric Equations of the Tilted Ellipse.

The parametric equations of a centered, non-tilted ellipse are simply expressed by:

$$x(\theta) = a \cos \theta \quad (1) \quad \text{and} \quad y(\theta) = b \sin \theta \quad (2)$$

The two parametric expressions (1) and (2) translate to mathematical terms the classical geometric construction of a *non-tilted* ellipse shown in Figure 2, where the ellipse is centered at the origin of the  $x, y$  reference-frame. In that classical geometric construction, two circles are first drawn, both centered at the origin, one with radius equal to the major semi-axis  $a$ , and respectively with radius equal to the minor semi-axis  $b$ .

Those two circles are then intersected at the points  $Q$  and  $R$  by a single radial line through the origin, drawn at an angle  $\theta$  relative to the abscissa  $x$ -axis. The point  $P$  of the centered, non-tilted ellipse that corresponds to the angular parameter  $\theta$  is then obtained as the intersection of the line through point  $Q$  orthogonal to the  $x$ -axis, and the line through point  $R$  orthogonal to the  $y$ -axis.

The parametric equations of a the *tilted*-ellipse, with major semi-axis  $a$ , minor semi-axis  $b$ , and tilt-angle  $\delta$ , centered at the origin of the  $\xi, \zeta$  Cartesian axes, are expressed by:

$$\xi(\theta) = (a \cos \delta) \cos \theta + (b \sin \delta) \sin \theta \quad (3)$$

$$\zeta(\theta) = (b \cos \delta) \sin \theta - (a \sin \delta) \cos \theta \quad (4)$$

where  $\theta$  is the ellipse angular-parameter, measured *counter-clockwise* starting from the  $x$ -axis, on the right-side of the ellipse major semi-axis  $a$ . As clearly shown in Figure 2, the angle  $\theta$  is however obviously not the polar angular-coordinate  $\varphi_{\xi\zeta}$  of the point  $(\xi, \zeta)$ , also measured *counter-clockwise*, but from the *positive*  $\xi$ -axis.

The angle  $\theta$  is also not the polar angular coordinate  $\varphi_{xy}$  of the point  $(x, y)$ , also measured *counter-clockwise*, from the *positive*  $x$ -axis, and related to the angle  $\theta$  by the transcendental trigonometric expression:

$$\varphi_{xy} = \arctan\left(\frac{y}{x}\right) = \arctan\left(\frac{b \sin \theta}{a \cos \theta}\right) = \arctan(\rho \tan \theta) \quad (5)$$

The parametric equations (3) and (4) of a tilted-ellipse may be directly derived from the corresponding parametric equations (1) and (2) of a centered, non-tilted ellipse, by applying a coordinate transformation that rotates the two ellipse axes  $\mathbf{x}$  and  $\mathbf{y}$  by the tilt-angle  $\delta$ . We assume here by convention the tilt-angle  $\delta$  to be positive in the *clockwise* rotation-sense.

The coordinate rotation may either be expressed by using a complex notation, as given by:

$$r = [\xi(z) + j\zeta(z)] \cdot e^{-j\delta} = (x \cos \delta + y \sin \delta) + (-x \sin \delta + y \cos \delta) \quad (6)$$

or equivalently in matrix-vector form, as shown by:

$$\begin{vmatrix} \xi(z) \\ \zeta(z) \end{vmatrix} = \begin{vmatrix} \cos \delta & \sin \delta \\ -\sin \delta & \cos \delta \end{vmatrix} \cdot \begin{vmatrix} x(z) \\ y(z) \end{vmatrix} \quad (7)$$

## 9. Vector-Addition Construction of the Tilted Ellipse.

The above-described classical geometric construction of the non-tilted ellipse has been correlated with the geometric construction of a centered, tilted-ellipse that is automatically generated by the vector-addition of a forward-wave vector  $V_{Fi}(\mathbf{z})$ , and of a backward-wave vector  $V_{Bi}(\mathbf{z})$ , while those two waves propagate, in opposing directions, along each virtual measurement-line connected a port  $i$  of the V-DUT multiport microwave-system under simulated test.

This second geometric construction is shown in Figure 4, and is characterized by the fact that, in a snapshot of the complex standing-wave field-pattern along each virtual measurement-line, the vector that represents the forward-wave rotates in phase in *counter-clockwise* sense, for increasing geometric distance  $\mathbf{z}$ , starting from the  $\mathbf{z} = 0$  line-end connected to the system port, towards the line-end connected to either the signal-source, or an auxiliary load. Similarly, the vector that represents the backward-wave rotates in phase *clockwise* for increasing distance  $\mathbf{z}$  from the V-DUT system port. The opposing directions of those two phase rotations are the obvious consequence of the fact that while the forward-wave increasingly *anticipates in phase* toward the source, the backward-wave increasingly *lags in phase* toward the source.

The process of vector-addition of a *counter-clockwise* rotating forward-wave vector  $V_{Fi}(\mathbf{z})$  and a *clockwise* rotating backward-wave vector  $V_{Bi}(\mathbf{z})$ , along each virtual measurement-line, makes the tip of the vector-sum  $V_i(\mathbf{z}) = V_{Fi}(\mathbf{z}) + V_{Bi}(\mathbf{z})$  trace the tilted-ellipse as an Hypotrochoid [5] (Figure 5).

The now-established mutual correlation between the two graphic constructions of a centered, tilted-ellipse leads to the determination of the mutual correspondence between the representative points  $(\xi, \zeta)$ , aligned around each ellipse, and the geometric locations  $\mathbf{z}$  along the corresponding virtual measurement-line. Indeed, we may easily conclude from Figure 5 that the radius-vector to each  $(\xi, \zeta)$  ellipse-point, measured from the origin of the  $(\xi, \zeta)$  system, represents the vector-sum  $V_i(\mathbf{z})$  of a forward-wave vector  $V_{Fi}(\mathbf{z})$ , and the corresponding backward-wave vector  $V_{Bi}(\mathbf{z})$ .



Further, the length of such radius-vector measures the local magnitude of the standing-wave field at the corresponding geometric locations  $\mathbf{z}$  along the measurement lines. Then clearly, the two ends of the ellipse major-axis cyclically correspond to the locations where the magnitude of the standing-wave-field is a maximum, while the two ends of the ellipse minor-axis cyclically correspond to the locations where the magnitude of the standing-wave-field is a minimum. Those are the geometric locations  $\mathbf{z}_{Mi}$  and  $\mathbf{z}_{mi}$  where the forward-wave vector  $\mathbf{V}_{Fi}(\mathbf{z})$ , and the corresponding backward-wave vector  $\mathbf{V}_{Bi}(\mathbf{z})$  respectively add in phase (*at a field-maximum  $\mathbf{z}_{Mi}$* ), and subtract in phase-opposition (*at a field-minimum  $\mathbf{z}_{mi}$* ), so that for those  $\mathbf{z}$ -locations we can write the two expressions:

$$a = \left| V_{Fi}(z) \right| + \left| V_{Bi}(z) \right| \quad (8)$$

$$b = \left| V_{Fi}(z) \right| - \left| V_{Bi}(z) \right| \quad (9)$$

and deduce from those expressions that the magnitudes of the forward and backward field-vectors are given by:

$$\left| V_{Fi}(z) \right| = \frac{1}{2} (a + b) \quad (10)$$

$$\left| V_{Bi}(z) \right| = \frac{1}{2} (a - b) \quad (11)$$

while the local value of the magnitude of the mutual wave-correlation-ratio is expressed by

$$\left| \Gamma_{ii}(z) \right| = \frac{a - b}{a + b} = \frac{1 - \rho}{1 + \rho} \quad (12)$$

where  $\rho$  measures the aspect ratio  $\rho = b/a$  of the ellipse minor semi-axis  $b$  to its major semi-axis  $a$ .

## 10. Expressions of the Inner-Angles.

As clearly shown in Figure 5, the Vectors  $\mathbf{V}_{Fi}(\mathbf{z})$ ,  $\mathbf{V}_{Bi}(\mathbf{z})$ , and the Vector-Sum  $\mathbf{V}_i(\mathbf{z})$  constitute the three sides of a plane triangle, so that the *Law of Cosines* of plane triangles may be applied to compute the three inner angles  $\alpha$ ,  $\beta$ , and  $\gamma$ , that are respectively opposite to the triangle sides  $\sigma$ ,  $\upsilon$ , and  $\tau$ :

$$\begin{aligned} \sigma &= \left| V(z) \right| = \sqrt{V_R^2(z) + V_I^2(z)} = \sqrt{\xi^2(z) + \zeta^2(z)} = \\ &= \sqrt{x^2(z) + y^2(z)} = x(z) \sqrt{1 + \left[ \frac{y(z)}{x(z)} \right]^2} = a \cos \theta \sqrt{1 + \rho^2 \tan^2 \theta} \end{aligned} \quad (13)$$

$$\mathfrak{v} = |V_B(z)| = \frac{1}{2}(a-b) = \sigma \frac{\sin \beta}{\sin \alpha} \dots \text{and} \dots \quad (14)$$

$$\tau = |V_F(z)| = \frac{1}{2}(a+b) = \sigma \frac{\sin \gamma}{\sin \alpha} \quad (15)$$

The expressions (13) to (15) of the cosines of the inner-angles  $\alpha$ ,  $\beta$ , and  $\gamma$  of that plane triangle are then:

$$\cos \alpha = \frac{1}{2\mathfrak{v}\tau}(\mathfrak{v}^2 + \tau^2 - \sigma^2) = \frac{\tau}{2\mathfrak{v}} \left[ 1 + \left( \frac{\mathfrak{v}}{\tau} \right)^2 - \left( \frac{\sigma}{\tau} \right)^2 \right] \quad (16)$$

$$\cos \beta = \frac{1}{2\sigma\tau}(\sigma^2 + \tau^2 - \mathfrak{v}^2) = \frac{\tau}{2\sigma} \left[ 1 + \left( \frac{\sigma}{\tau} \right)^2 - \left( \frac{\mathfrak{v}}{\tau} \right)^2 \right] \quad (17)$$

$$\cos \gamma = \frac{1}{2\sigma\mathfrak{v}}(\sigma^2 + \mathfrak{v}^2 - \tau^2) = \frac{\tau^2}{2\sigma\mathfrak{v}} \left[ \left( \frac{\sigma}{\tau} \right)^2 + \left( \frac{\mathfrak{v}}{\tau} \right)^2 - 1 \right] \quad (18)$$

The expressions (16) to (18) of the three inner-angle cosines may be cast in the form of explicit functions of the tilted-ellipse angular-parameter  $\Theta$ , by substituting in the respective second forms the sixth form of (13), and the second forms of (14) and (15).

Quite clearly, only the ratio  $\sigma / \tau$  is actually a function of the tilted-ellipse angular-parameter  $\Theta$ , in the second forms of the three inner-angle cosines (16) to (18), while the ratio  $\mathfrak{v} / \tau$  is actually a constant that expresses the magnitude of the wave-correlation-ratio  $|\Gamma_{ii}|$ , as given by the expression (12).

Those substitutions lead, after appropriate simplifications, to the following expressions (19) to (21) of the three inner-angle cosines, cast in the form of explicit functions of the tilted-ellipse angular-parameter  $\Theta$ :

$$\cos \alpha = -\cos 2\Theta \quad (19)$$

$$\cos \beta = \frac{1 - (1 - \rho) \sin^2 \Theta}{\sqrt{1 - (1 - \rho^2) \sin^2 \Theta}} \quad (20)$$

$$\cos \gamma = \frac{1 - (1 + \rho) \sin^2 \Theta}{\sqrt{1 - (1 - \rho^2) \sin^2 \Theta}} \quad (21)$$

Most remarkably, the expression (19) of cosine  $\alpha$  shows that the angle  $\alpha$  linearly increases (or decreases) at twice the rate of the ellipse angular-parameter  $\Theta$ , consistently with the span of the angle  $\alpha$  extending between the Forward-Wave vector  $V_{Fi}(\mathbf{z})$ , that linearly leads in phase, and the Backward-Wave vector  $V_{Bi}(\mathbf{z})$ ,

that linearly lags in phase, for increasing distance  $z$  from the  $z = 0$  line-end connected to the V-DUT port, towards the line-input connected to the signal-source.

## 11. Expressions of the Forward-Wave and Backward-Wave Phase-Angles.

The magnitudes of the Forward-Wave Vectors  $|V_{Fi}(z)|$ , and Backward-Wave Vectors  $|V_{Bi}(z)|$ , as well as the magnitudes of the Wave-Correlation-Ratios  $|\Gamma_{ii}|$ , and  $|\Gamma_{ij}|$  are all constant along each of the virtual measurement-lines, because of those lines being simulated uniform and lossless. The assumptions of uniformity and losslessness leads to the very simple expressions (10) to (12), that directly relate those magnitudes to the lengths of the two tilted-ellipse semi-axes  $a$  and  $b$ , and to the tilted-ellipse aspect-ratio  $\rho$ .

Quite to the contrary, the phase-angles  $\varphi_F(z)$  of the Forward-Wave, and  $\varphi_B(z)$  of the Backward-Wave are both linear functions of the distance  $z$  from the line-end connected to a V-DUT port :

$$\varphi_F(z) = \varphi_F(0) + \frac{2\pi}{\lambda} z \quad (22)$$

$$\varphi_B(z) = \varphi_B(0) - \frac{2\pi}{\lambda} z \quad (23)$$

while the phase-angle of the Wave-Correlation-Ratios  $\Gamma_{ii}$  is given by:

$$\varphi_\Gamma(z) = \varphi_B(z) - \varphi_F(z) = \varphi_\Gamma(0) - \frac{4\pi}{\lambda} z \quad (24)$$

The *a-priori* knowledge of the linear dependence of the phase-angles  $\varphi_F(z)$ , and  $\varphi_B(z)$ , expressed by (22) and (23), provides a simple way to compute the values of the two phase-angles  $\varphi_F(0)$ ,  $\varphi_B(0)$ , and of the phase-angle  $\varphi_\Gamma(0)$ , at the locations  $z = 0$  of each V-DUT port, that are required to obtain the values of the complex diagonal elements  $S_{ii} = \Gamma_{ii}$ , and of the off-diagonal element  $S_{ij} = \Gamma_{ij}$  of the V-DUT scattering matrix. The determination of the phase-angles  $\varphi_F(0)$ ,  $\varphi_B(0)$  is indeed simple, provided at least one value of the phase-angles  $\varphi_F(z)$ , and  $\varphi_B(z)$  is known, at a known location  $z = z_i$  of each line.

The values of the phase-angles  $\varphi_F(z)$ , and  $\varphi_B(z)$  at any location  $z$  may however be different, depending upon which relatively-arbitrary ellipse-reference-point is used. It is therefore necessary to distinguish among those different values, by using different symbols. In the following discussion, the symbols  $\varphi_{F\xi\zeta}$  and  $\varphi_{B\xi\zeta}$  will represent the phase-angles  $\varphi_F$ , and  $\varphi_B$ , measured *counter-clockwise* and respectively *clockwise*, from the *positive*  $\xi$ -axis. Similarly, the symbols  $\varphi_{Fxy}$  and  $\varphi_{Bxy}$  will represent the phase-angles  $\varphi_F$ , and  $\varphi_B$ , measured *counter-clockwise* and respectively *clockwise*, from the *positive*  $x$ -axis.

The known expression (20) of the cosine of the inner-angle  $\beta$  is then quite useful for expressing the phase-angles  $\varphi_{Fxy}$ , as function of both the polar-angle  $\varphi_{xy}$  of the point  $(x, y)$ , and the inner-angle  $\beta$ .

Indeed, as is easy to see in Figure 6, within the *first* and *third* quadrants of the ellipse, where  $0 \leq \theta \leq \pi/2$  and  $\pi \leq \theta \leq 3\pi/2$ , the phase-angle  $\varphi_{Fxy}$  of the Forward Wave  $V_{Fi}(\mathbf{z})$ , as seen in the  $\mathbf{x}$ - $\mathbf{y}$  reference-frame, *appears* to be expressed by:

$$\varphi_{Fxy1} = \varphi_{xy} + \beta \quad (25)$$

Similarly, as is easy to see in Figure 7, within the *second* and *fourth* quadrants of the ellipse, where  $\pi/2 \leq \theta \leq \pi$  and  $3\pi/2 \leq \theta \leq 2\pi$ , the phase-angle  $\varphi_{Fxy}$  of the Forward Wave  $V_{Fi}(\mathbf{z})$ , as seen in the  $\mathbf{x}$ - $\mathbf{y}$  reference-frame, *appears* to be expressed by:

$$\varphi_{Fxy2} = \varphi_{xy} - \beta \quad (25^a)$$

The two expressions (25) and (25<sup>a</sup>) may however be reduced to just the expressions (25), by defining the angle  $\beta$  as being oriented *from* the Forward-Wave Vector  $V_{Fi}(\mathbf{z})$  ( represented by the triangle-side  $\tau$  ), *towards* the Vector-Sum  $V_i(\mathbf{z})$  ( represented by the triangle-side  $\sigma$  ), and by considering it to be *positive* when extending in *counter-clockwise* sense, and to be *negative* when extending in *clockwise* sense.

As a consequence of that convention, the inner-angle  $\beta$  becomes automatically *positive* within the *first* and *third* quadrants of the ellipse, and *negative* within the *second* and *fourth* quadrants, thus making the use of two different expressions unnecessary. The phase-angle  $\varphi_{Fxy}$  may then be expressed by the single expression (25).

Further, that sign-convention is also consistent with the expression of the inner-angle  $\beta$  as  $\arctan(\tan \beta)$ , where the expression of  $\tan \beta$  may be simply derived from that in (20) of  $\cos \beta$ , and is given by :

$$\tan \beta = \frac{\sqrt{1 - \cos^2 \beta}}{\cos \beta} = \frac{(1 - \rho) \sin \theta \cos \theta}{1 - (1 - \rho) \sin^2 \theta} \quad (26)$$

The above-established sign-convention for the inner-angle  $\beta$  is further also consistent with the other expression of  $\tan \beta$ , that is obtained by first solving the expression (5<sup>a</sup>), of the tangent of the angle  $\varphi_{xy}$ , for the ellipse aspect-ratio  $\rho$  :

$$\tan \varphi_{xy} = \frac{y}{x} = \frac{b \sin \theta}{a \cos \theta} = \rho \tan \theta \quad (5^a)$$

$$\rho = \frac{\tan \varphi_{xy}}{\tan \theta} \quad (5^b)$$

and by substituting the expression (5<sup>b</sup>) of the ellipse aspect-ratio  $\rho$  in the expression (26) of  $\tan \beta$ . That substitution leads, with appropriate simplifications, to the expression:

$$\tan \beta = \frac{\left(1 - \frac{\tan \varphi_{xy}}{\tan \theta}\right) \sin \theta \cos \theta}{1 - \left(1 - \frac{\tan \varphi_{xy}}{\tan \theta}\right) \sin^2 \theta} = \frac{\tan \theta - \tan \varphi_{xy}}{1 + \tan \theta \tan \varphi_{xy}} = \tan(\theta - \varphi_{xy}) \quad (26^a)$$

The expression (26<sup>b</sup>) of  $\tan \beta$  shows that the inner-angle  $\beta$  is actually correctly expressed by :

$$\beta = \theta - \varphi_{xy} \quad (25^a)$$

which clearly confirms that indeed the phase-angle  $\varphi_{Fxy}$  of the Forward-Wave vector  $V_{Fi}(\mathbf{z})$ , as seen in the  $\mathbf{x}\text{-}\mathbf{y}$  reference-frame, is *identical* to the tilted-ellipse angular parameter  $\theta$ . Figure 9 shows overlay-plots of the inner-angle  $\beta$ , with its sign set by the given convention, of the angle  $\varphi_{xy}$ , and of the phase-angle  $\varphi_{Fxy}$ , all three angles being displayed as functions of the tilted-ellipse angular-parameter  $\theta$  ( in all such graphics displays, the numerical values of the tilted-ellipse parameters are assumed to be:  $\rho = 1/4$ , and  $\delta = 30^\circ$  ).

A further confirmation of the expression (25) of the phase-angle  $\varphi_{Fxy}$  may be obtained by computing the expressions of its sine, its cosine, and its tangent given by:

$$\sin \varphi_{Fxy} = \cos(\varphi_{xy} + \beta) = \sin \varphi_{xy} \cos \beta + \cos \varphi_{xy} \sin \beta \quad (27)$$

$$\cos \varphi_{Fxy} = \cos(\varphi_{xy} + \beta) = \cos \varphi_{xy} \cos \beta - \sin \varphi_{xy} \sin \beta \quad (28)$$

$$\tan \varphi_{Fxy} = \frac{\tan \varphi_{xy} + \tan \beta}{1 - \tan \varphi_{xy} \tan \beta} \quad (29)$$

The expressions (27) to (28) may also be cast in the form of explicit functions of the ellipse angular-parameter  $\theta$ , by substituting the expressions of the sine, cosine, and tangent of the polar angle  $\varphi_{xy}$  :

$$\sin \varphi_{xy} = \frac{y}{\sigma} = \frac{b \sin \theta}{a \cos \theta \sqrt{1 - \rho^2 \tan^2 \theta}} = \frac{\rho \tan \theta}{\sqrt{1 - \rho^2 \tan^2 \theta}} \quad (30)$$

$$\cos \varphi_{xy} = \frac{x}{\sigma} = \frac{a \cos \theta}{a \cos \theta \sqrt{1 - \rho^2 \tan^2 \theta}} = \frac{1}{\sqrt{1 - \rho^2 \tan^2 \theta}} \quad (31)$$

$$\tan \varphi_{xy} = \rho \tan \theta \quad (32)$$

and that of the sine, cosine, and tangent of the inner-angle  $\beta$ , the being cosine given by (20), and the sine by:

$$\sin \beta = \sqrt{1 - \cos^2 \beta} = \frac{(1 - \rho) \sin \theta \cos \theta}{\sqrt{1 - (1 - \rho^2) \sin^2 \theta}} \quad (33)$$

Those substitutions lead, after appropriate simplifications, to expressions of the sine, cosine and tangent of the phase angle  $\varphi_{Fxy}$  of the Forward Wave  $V_{Fi}(\mathbf{z})$ , as seen in the  $\mathbf{x}\text{-}\mathbf{y}$  reference-frame, as explicit functions of the tilted-ellipse angular-parameter  $\theta$  :

$$\sin \varphi_{Fxy} = \tan \theta \sqrt{\frac{1 - (1 - \rho^2) \sin^2 \theta}{1 + \rho^2 \tan^2 \theta}} = \sqrt{\sin^2 \theta} \quad (34)$$

$$\cos \varphi_{Fxy} = \sqrt{\frac{1 - (1 - \rho^2) \sin^2 \theta}{1 + \rho^2 \tan^2 \theta}} = \sqrt{\cos^2 \theta} \quad (35)$$

$$\tan \varphi_{Fxy} = \tan \theta \quad (36)$$

Most remarkably, the graphic display in Figure 10, of the transcendental functional relations (34) to (36), that express the sine, cosine, and tangent of the phase angle  $\varphi_{Fxy}$  of the Forward-Wave Vector, as explicit functions of the tilted-ellipse angular-parameter  $\theta$ , clearly shows that the phase angle  $\varphi_{Fxy}$  is, in the  $\mathbf{x}\text{-}\mathbf{y}$  reference-frame, indeed *identical* to the angular-parameter  $\theta$  :

$$\varphi_{Fxy} = \varphi_{xy} + \beta = \theta \quad (37)$$

## 12. The Tilted-Ellipse Cardinal Points.

The angles  $\varphi_{Fxy}$  and  $\theta$  are then both zero on the positive-side of the  $\mathbf{x}$ -axis, and in particular at the positive-end of the major semi-axis  $\mathbf{a}$ , where the magnitude  $|V_i(\mathbf{z})|$  of the standing-wave pattern is a maximum. The positive-end of the major semi-axis  $\mathbf{a}$ , where  $\xi = \mathbf{a} \cos \delta$  and  $\zeta = -\mathbf{a} \sin \delta$ , corresponds then to the locations  $\mathbf{z} = \mathbf{z}_{Mi}$  of each virtual measurement-line where the magnitude  $|V_i(\mathbf{z})|$  of the standing-wave pattern is a maximum, because of the Forward-Wave Vector  $V_{Fi}(\mathbf{z})$ , and the Backward-Wave Vector  $V_{Bi}(\mathbf{z})$  locally adding in-phase. Similarly, the angles  $\varphi_{Fxy}$  and  $\theta$  are both equal to  $\pi$  on the negative-side of the  $\mathbf{x}$ -axis, so that the negative-end of the major semi-axis  $\mathbf{a}$ , where  $\xi = -\mathbf{a} \cos \delta$  and  $\zeta = \mathbf{a} \sin \delta$ , corresponds to the locations  $\mathbf{z} = \mathbf{z}_{M(i+I)}$  of each virtual measurement-line, where the Forward-Wave Vector  $V_{Fi}(\mathbf{z})$ , and the Backward-Wave Vector  $V_{Bi}(\mathbf{z})$  are again adding in-phase, because  $V_{Fi}(\mathbf{z})$  having rotated *counter-clockwise* by  $+\pi$ , and  $V_{Bi}(\mathbf{z})$  having rotated *clockwise* by  $-\pi$ , relative to  $\mathbf{z} = \mathbf{z}_{Mi}$ .

The distance from point  $\mathbf{z} = \mathbf{z}_{Mi}$  to point  $\mathbf{z} = \mathbf{z}_{M(i+I)}$  is quite obviously equal to one-half of the known wavelength  $\lambda$  of the common forward-, and backward-wave mode, used for exciting the given V-DUT port.

Further, the angles  $\varphi_{Fxy}$  and  $\theta$  are both are equal to  $\pi/2$ , and respectively  $3/2 \pi$  at the positive and negative ends of the ellipse *minor* semi-axis  $\mathbf{b}$ , where  $y = \pm \mathbf{b}$  and the magnitude  $|V_i(\mathbf{z})|$  of the standing-wave pattern is a minimum.

The positive and negative ends of the minor semi-axis  $\mathbf{b}$ , where  $\xi = \pm \mathbf{b} \sin \delta$  and  $\zeta = \pm \mathbf{b} \cos \delta$ , corresponds then to the locations  $\mathbf{z} = \mathbf{z}_{mi}$  and  $\mathbf{z} = \mathbf{z}_{m(i+1)}$  of each virtual measurement-line, where the magnitude  $|V_i(\mathbf{z})|$  of the standing-wave pattern is a minimum, due to the Forward-Wave Vector  $V_{Fi}(\mathbf{z})$ , and the Backward-Wave Vector  $V_{Bi}(\mathbf{z})$  locally adding in phase-opposition.

### 13. Angular-Parameters and Electric-Distances.

The positive and negative ends of the major and minor semi-axes are therefore cardinal points of the tilted-ellipse, where the values of the angles  $\varphi_{Fxy}$  and  $\theta$  have very simple known values of either zero or a integer multiple of  $\pi/2$ . Unfortunately, the corresponding geometrical locations  $\mathbf{z} = \mathbf{z}_{Mi}$  and  $\mathbf{z} = \mathbf{z}_{mi}$ , along each virtual measurement-line, can not be accurately determined, because of the local slope of the standing-wave field-magnitude  $|V_i(\mathbf{z})|$  being zero at both a maximum, and at a minimum. Indeed, the only the  $(\xi, \zeta)$  or  $(x, y)$  points of the tilted-ellipse, that correspond to known geometrical locations along each virtual measurement-line, are the  $n$  points identified by  $\theta = \theta(\mathbf{z}_i)$  (for  $i = 1, 2 \dots n$ ), that are aligned on the same straight-lines through the origin, with the  $n$  points that represent, in the  $(\xi, \zeta)$  reference-frame, the standing-wave field-values used as inputs for the least-squares ellipse-fitting algorithm.

The  $n(\xi, \zeta)$  points, used as inputs for the least-squares ellipse-fitting algorithm, are those obtained from the  $n$  known, equidistant geometrical-locations  $\mathbf{z}_i$ , selected along a segment of virtual measurement-line, sufficiently removed from the V-DUT port so that the evanescent higher-order modes that affect the line-to-port transition are decayed to negligible magnitudes. Those  $n(\xi, \zeta)$  points are identified by  $n$  values  $\theta(\mathbf{z}_i)$  of the tilted-ellipse angular-parameter  $\theta$ , and by the  $n$  corresponding values  $\psi(\mathbf{z}_i) = (2\pi \mathbf{z}_i)/\lambda$  of the electrical distance, from the specific V-DUT port at the downstream line-end.

As a consequence, the  $n(\xi, \zeta)$  points of the tilted-ellipse that are aligned on the same straight-lines through the origin and very close to those representing the least-squares ellipse-fitting algorithm inputs, are identified by the same  $n$  values  $\theta(\mathbf{z}_i)$  of the angular-parameter  $\theta$ , and may be assumed to closely correspond to the same  $n$  known, equidistant geometrical-locations  $\mathbf{z}_i$ . Those ellipse points provide then the most accurate one-to-one mapping of all values of the angular-parameter  $\theta$ , onto all geometrical locations  $\mathbf{z}$ , and onto all the corresponding values of the electrical distance  $\psi(\mathbf{z})$ , including in particular those of the four cardinal points, at the positive and negative ends of the major and minor ellipse-axes.

That one-to-one mapping of all values of the angular-parameter  $\theta$ , onto all geometrical locations  $\mathbf{z}$  along each of the measurement-lines, leads then to simple, obvious expressions of the values of the phase-angles of the forward and backward wave  $\varphi_F(\mathbf{0})$ ,  $\varphi_B(\mathbf{0})$ , and of the phase-angle of the complex wave-correlation-ratios  $\varphi_\Gamma(\mathbf{0})$ , at the locations  $\mathbf{z} = 0$  of each V-DUT port:

$$\varphi_{Fxy}(0) = \varphi_{Fxy}(z_i) - \frac{2\pi}{\lambda} z_i \quad (38)$$

$$\varphi_{Bxy}(0) = \varphi_{Bxy}(z_i) + \frac{2\pi}{\lambda} z_i \quad (39)$$

Work in progress:

---

Expression of the Phase-Angles  $\varphi_{F\xi\zeta}(z)$ , and  $\varphi_{B\xi\zeta}(z)$  of the FW and BW.

(Work in progress: Check the expressions in the following paragraphs !)

Further, it is easy to see in Figure 4, that, the phase angle  $\varphi_F(z)$  of the Forward Wave  $V_{Fi}(z)$ , in the  $\xi$ - $\zeta$  reference-frame is expressed by:

$$\varphi_{F\xi\zeta}(z) = \varphi_{\xi\zeta}(z) + \beta(z) = \varphi_{xy}(z) - \delta + \beta(z) \quad (40)$$

Similarly, it is easy to see in Figure 4, that the phase angle  $\varphi_B(z)$  of the Backward Wave  $V_{Bi}(z)$  in the  $\xi$ ,  $\zeta$  reference-frame is expressed by:

$$\varphi_{B\xi\zeta}(z) = -\left[ \varphi_{\xi\zeta}(z) + \beta + 2\delta \right] \quad (41)$$


---

### Line-to-Line Correlation.

Quite obviously, if  $i \neq j$  the expressions (9) and (10) would become:

$$|V_{Fi}(z)| = \frac{1}{2}(a_i + b_i) \quad (9^a)$$

$$|V_{Bj}(z)| = \frac{1}{2}(a_j - b_j) \quad (10^a)$$

and the expression (11) would then become:

$$|\Gamma_{ij}(z)| = \frac{|V_{Bj}|}{|V_{Fi}|} = \frac{a_j - b_j}{a_i + b_i} = \frac{a_j}{a_i} \frac{1 - \rho_j}{1 + \rho_i} = \chi_{ij} \frac{1 - \rho_j}{1 + \rho_i} \quad (11^a)$$

where the variable  $\chi$  measures the ratio  $\chi = a_j/a_i$  of the two ellipses major-axes  $a_j$  and  $a_i$ , and represents a scaling-factor relating the tilted-ellipse of line  $j$  to that of line  $i$ .

The latter points are characterized by the geometric distance  $z$  from the system port, and by the corresponding electrical distance  $\psi(z) = 2\pi z/\lambda$ .

---





## 14. Conclusions.

This paper provides a fairly detailed description of a new method that has the capability of simulating calibrated-measurements of complex, multi-dimensional scattering-matrices. The method described does not require the simulation of a full physical, multi-port, automated vector network-analyzer (VANA). The only requirement is the extension of the domain of a complex EM-field solution to include the inner regions of short lengths of *virtual* measurement transmission-lines (*or waveguides*). The *virtual* measurement-lines are assumed to be uniform, and lossless, but not-necessarily non-dispersive. Those virtual lines are simulated as being connected to the multiport system under test, exactly as physical measurement-lines would be connected, in an experimental vector network analyzer set-up. At every step of the simulated measurement-cycle, a stepped-frequency sine-wave signal is assumed to be fed towards one of the ports of the system under test. During the full measurement-cycle the stepped frequency sine wave excitation signal is progressively switched towards a different port of the system under test, through a different *virtual* measurement-line. Uncalibrated values of the scattering parameters are then obtained by first extracting the values of the real and imaginary components of the standing-wave field, along each of the *virtual* measurement lines, obtained from a *complex* electromagnetic-field Maxwell-solver.

The field samples are extracted at a set of line locations spaced at regular distance increments, from the reference point that marks the location of a test-system port. The *a-priori*-known tilted-ellipse shape of the 2D display of the *imaginary* standing-wave-field component, as function of the corresponding *real* component, is then used in a least-squares ellipse-fitting algorithm, that computes the lengths of the two ellipse semi-axes, and the value of the tilt-angle of the ellipse major axis, with respect to the abscissa-axis.

The set of equidistant line locations, where the *real* and *imaginary* components of standing-wave-field are extracted, must cover a line-segment that is sufficiently removed from the system port, so that the superimposed, local evanescent higher-modes, that affect the line-to-system transition, are decayed to very low magnitudes, thus assuring that only the single mode, required for the excitation of the given specific port, is propagating where field-data are being collected. That line segment should cover a number of line-wavelengths.

The three geometric parameters of the tilted-ellipse that corresponds to each virtual measurement-line, obtained from the least-squares ellipse-fitting algorithm, may be directly used to compute the *amplitudes* and *phases* of the forward-wave- , and backward-wave-vectors. The new simulation method extracts thus the complex values of the two waves that propagate, in opposing directions, along each measurement-line, performing thus a wave-extraction-function that would require, in an experimental setting, a hardware vector-reflectometer inserted along each line. The wave-correlation-ratios between each backward-wave-vector and all forward-wave-vectors represent either uncalibrated reflection coefficients, or uncalibrated transmission coefficients, depending upon whether the two waves selected propagate along the same virtual measurement-line or along different lines. Multi-port calibration procedures can be also simulated, by replacing the system under test with an sufficient number of calibration standards, each having a postulated scattering-response.

The physical cross-section geometry of the virtual measurement-lines, and the type of complex field-solver used are completely arbitrary, and different solvers may be used while repeating the same simulation. The relative accuracy of the various solvers used may then be determined, by mutually comparing the residual least-squares errors, and the system-error descriptions generated by the calibration procedure, both errors being obtained using arrays of input EM-field values, having equal numbers of elements.

## 15. References.

- [1] Speciale, R. A., "Computer Simulation of Scattering Parameter Measurements," Expanded Monograph of this same paper, available for downloading from: <http://home.comcast.net/~rspeciale/>.
- [2] Speciale, R. A., "Multiport Network Analyzers," Microwave System News, Vol. 10, N0. 6, June 1980, pp. 67-89.
- [3] Speciale, R. A., "Super-TSD. A Generalization of the TSD Network Analyzer Calibration Procedure, Covering n-Port Measurements with Leakage," in 1977 IEEE-MTT-S International Microwave Symposium Digest of Technical Papers (San Diego, CA) pp. 114-117, June 21-23, 1977, IEEE Catalog No. 77CH1219-5 MTT.
- [4] Speciale, R. A., "Generalization of the TSD Network Analyzer Calibration Procedure, covering n-Port Measurements with Leakage," IEEE Trans. on Microwave Theory and Techniques, in Vol. MTT-25, No. 12, pp. 1100-1115, December 1977.
- [5] Xah Lee , "Special Plane Curves," available for downloading from:  
[http://www.xahlee.org/SpecialPlaneCurves\\_dir/Ellipse\\_dir/ellipse.html](http://www.xahlee.org/SpecialPlaneCurves_dir/Ellipse_dir/ellipse.html)
- [6] Agilent Technologies, Inc. , "Test Solutions for Multiport and Balanced Devices," Publication number 5988-2461EN, May 11, 2001.
- [7] Anritsu Application Note/GIP-B, No. 11410-00279, "Three and Four Port S-parameter Measurements - Calibrations and Mixed-Mode Parameters," (Scorpion), November 2001, Rev: A.
- [8] Gander, W., Golub, G. H. and Strebel R., "Least-square fitting of circles and ellipses," BIT, 43:558-578, 1994.
- [9] Radim Halir ( and Jan Flusser, "Numerically Stable Direct Least Squares Fitting of Ellipses," in Axel Pinz, editor, Proc. of the 20th Workshop of the Austrian Association for Pattern Recognition (OAGM'96), pages 251-261, Schloss Seggau, Leibnitz, May 1996.



# APPENDIX - 1

## Graphic Displays of the Tilted-Ellipse Representation of Standing-Wave Patterns

*( Including the Vector-Addition Triangle  
and its Inner-Angles  $\alpha$ ,  $\beta$ , and  $\gamma$  ).*



## Figure Captions.

FIGURE 1 - Phased-Array in a Near-Field Scanner.

FIGURE 2 - Analytic Geometry of the Tilted Ellipse.

FIGURE 3 - The Tilted-Ellipse Representation of a Standing-Wave Pattern.

FIGURE 4 - The Tilted-Ellipse Representation of a Standing-Wave Pattern: Vector-Addition Triangles in the First and Third Quadrants.

FIGURE 5 - The Tilted-Ellipse Representation of a Standing-Wave Pattern: Vector-Addition Triangles in the Second and Fourth Quadrants.

FIGURE 6 - Detail of the Vector-Addition Triangles in the First Quadrant.

FIGURE 7 - Detail of the Vector-Addition Triangles in the Second Quadrant.

FIGURE 8 - Detail of the Vector-Addition Triangles in the First Quadrant: Angle  $\theta = \varphi_{xy} + \beta$ .

FIGURE 9 - TBD.



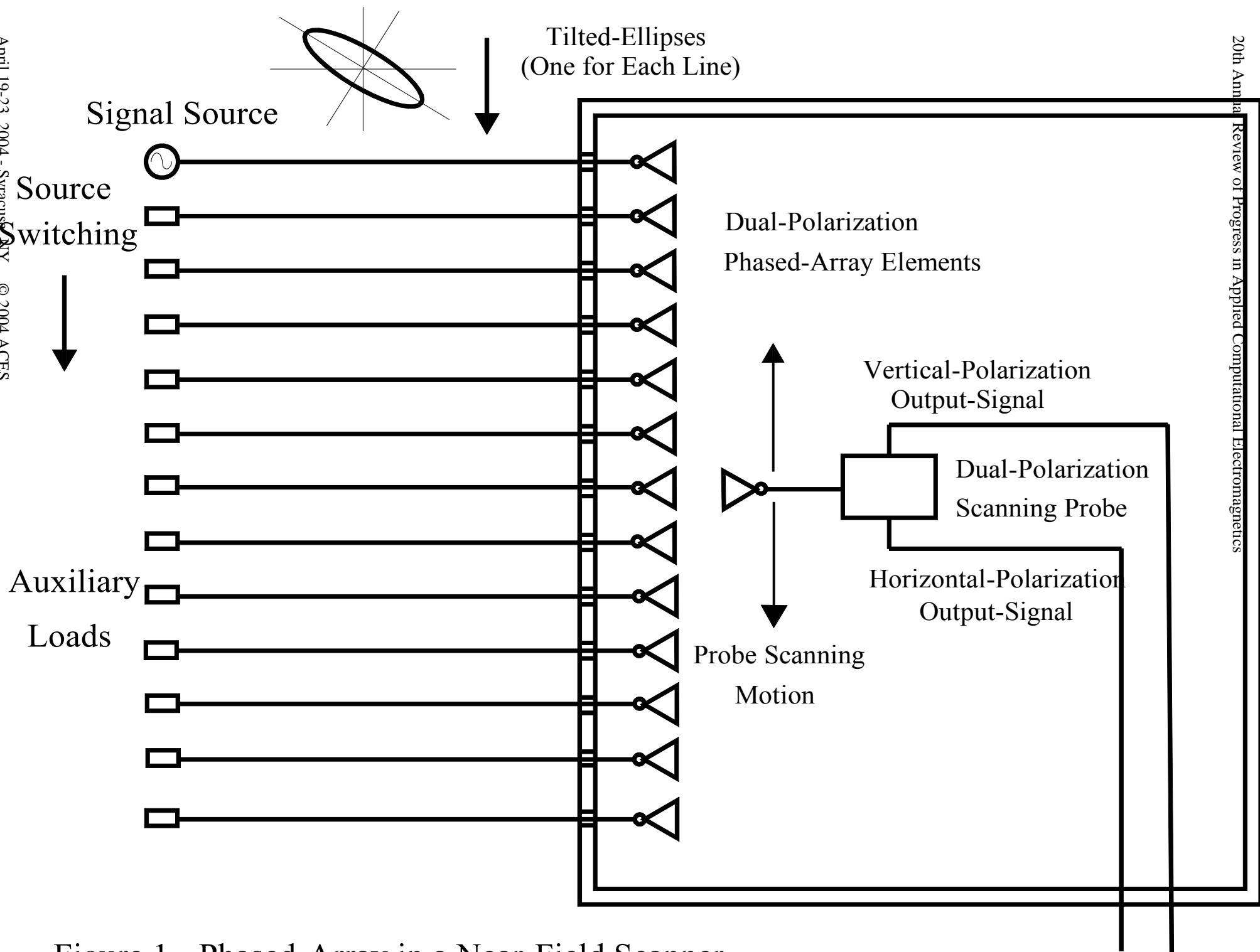


Figure 1 - Phased-Array in a Near-Field Scanner.

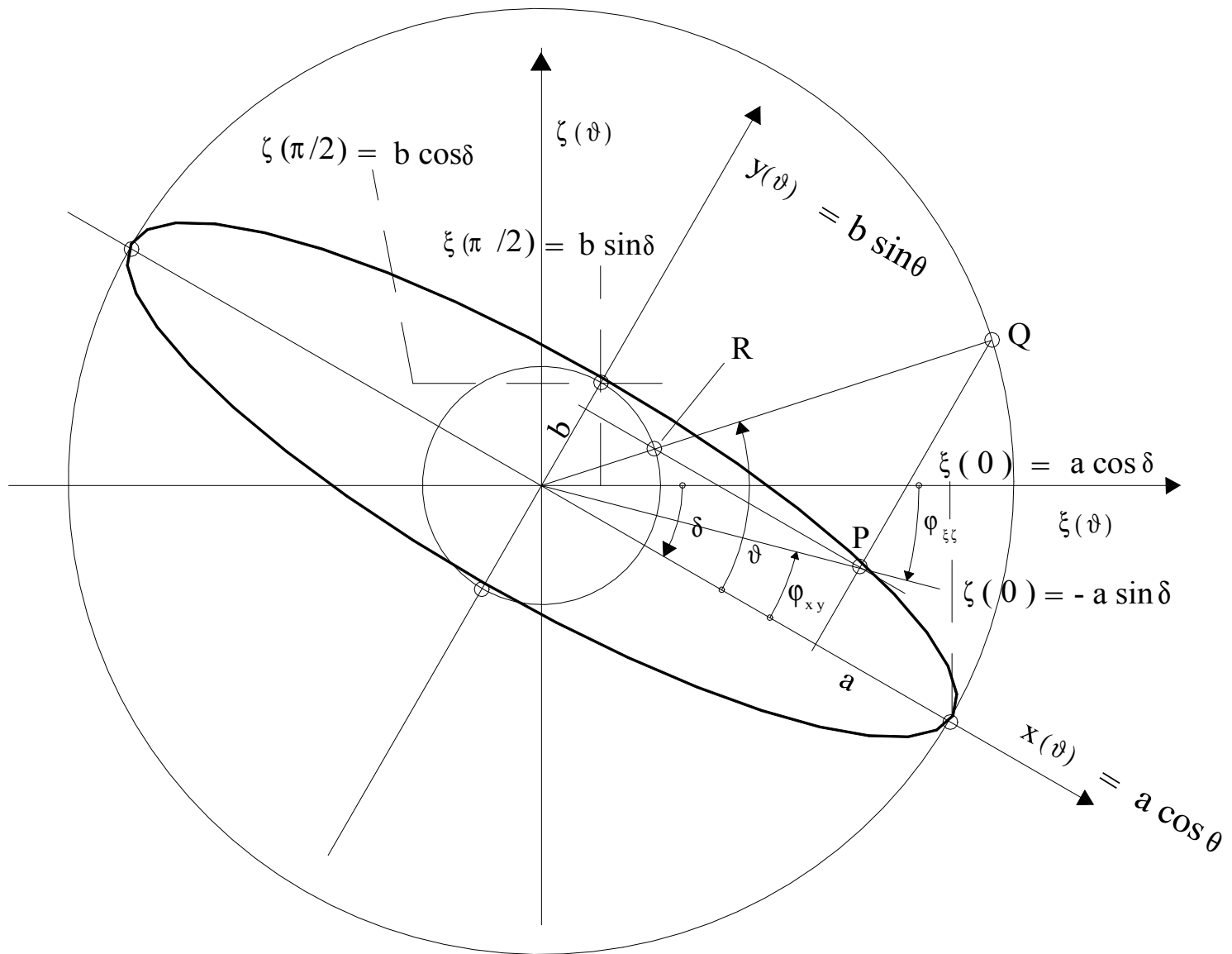
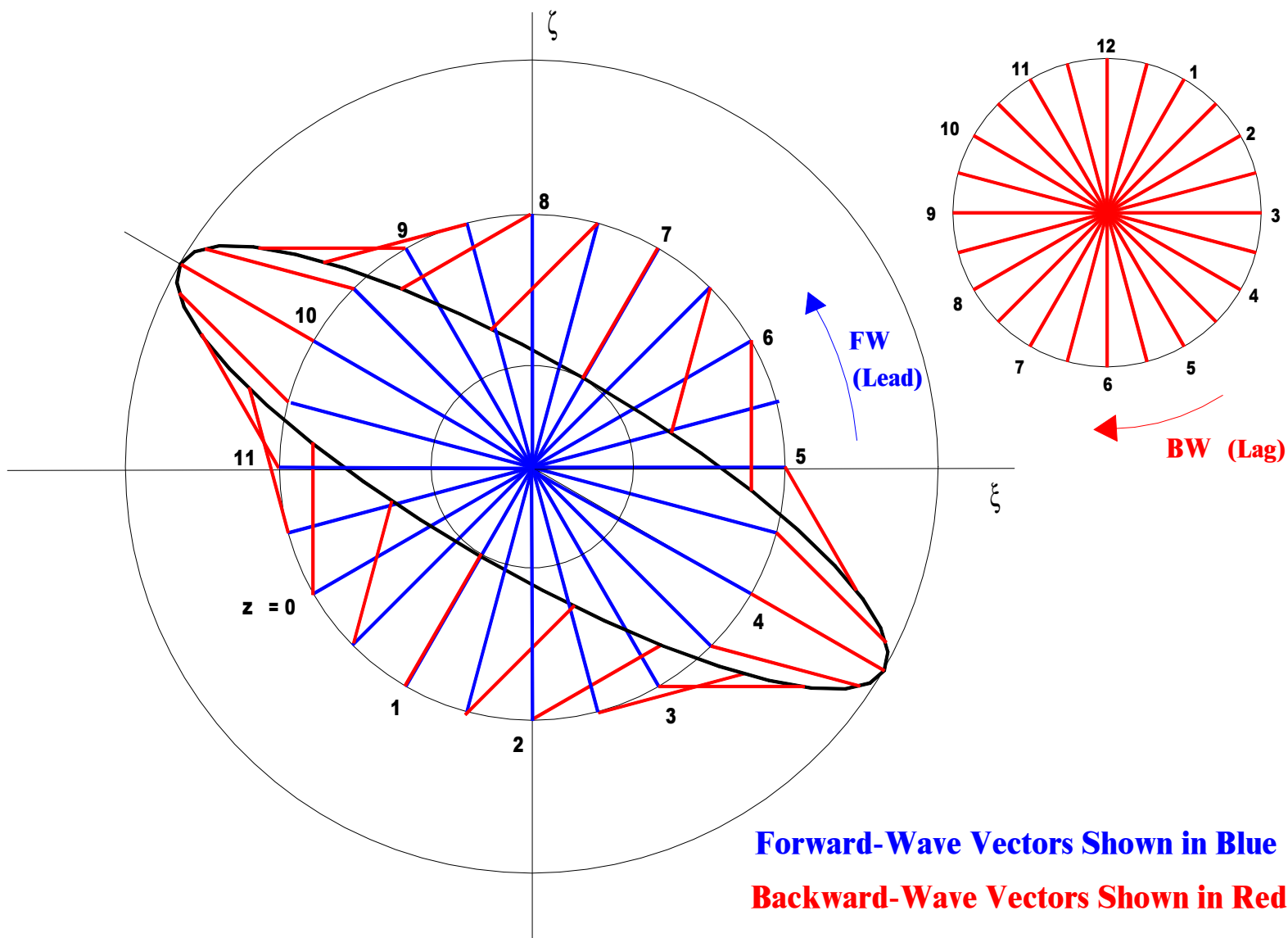
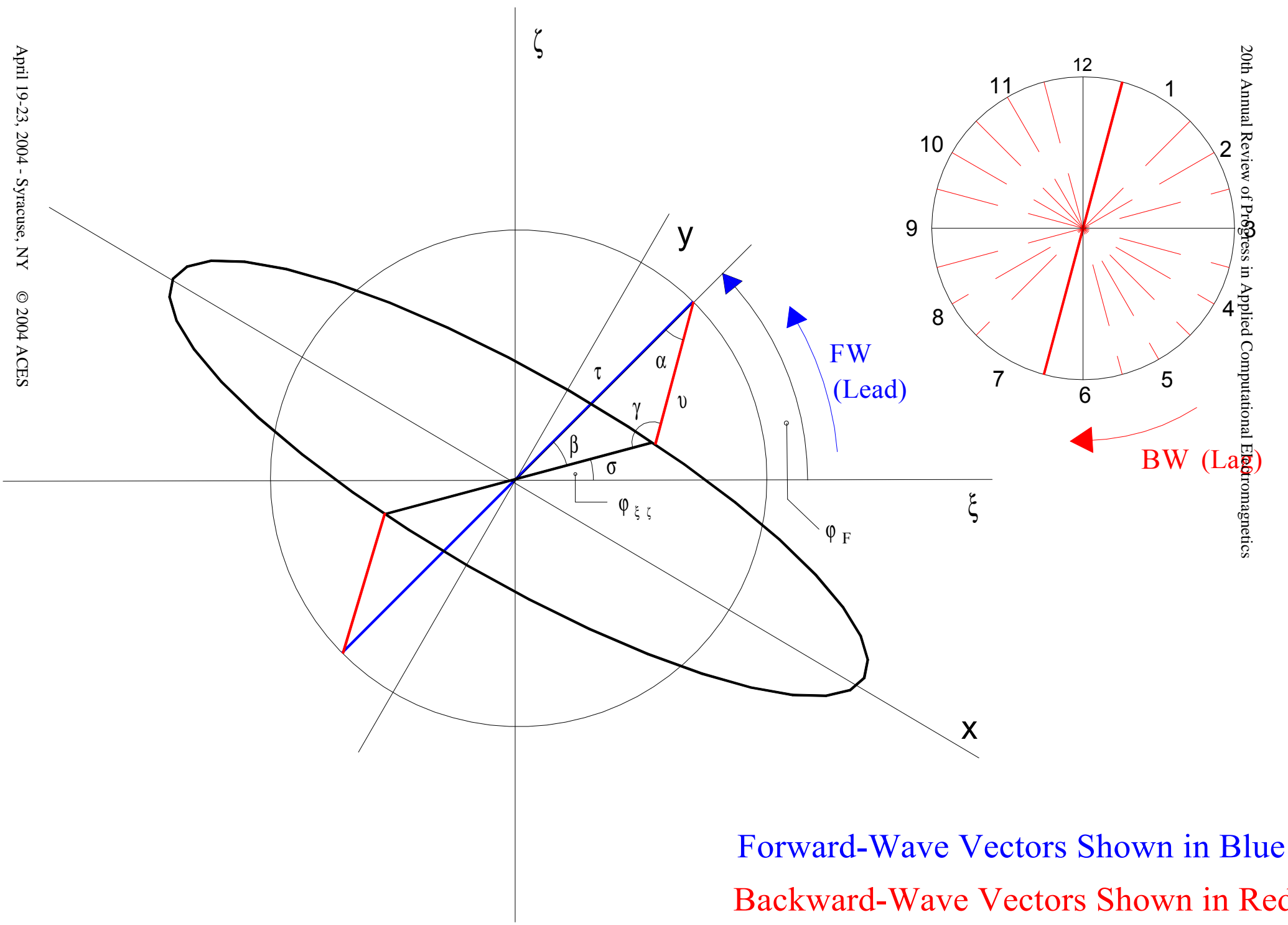


Figure 2 - Analytic Geometry of the Slanted Ellipse.



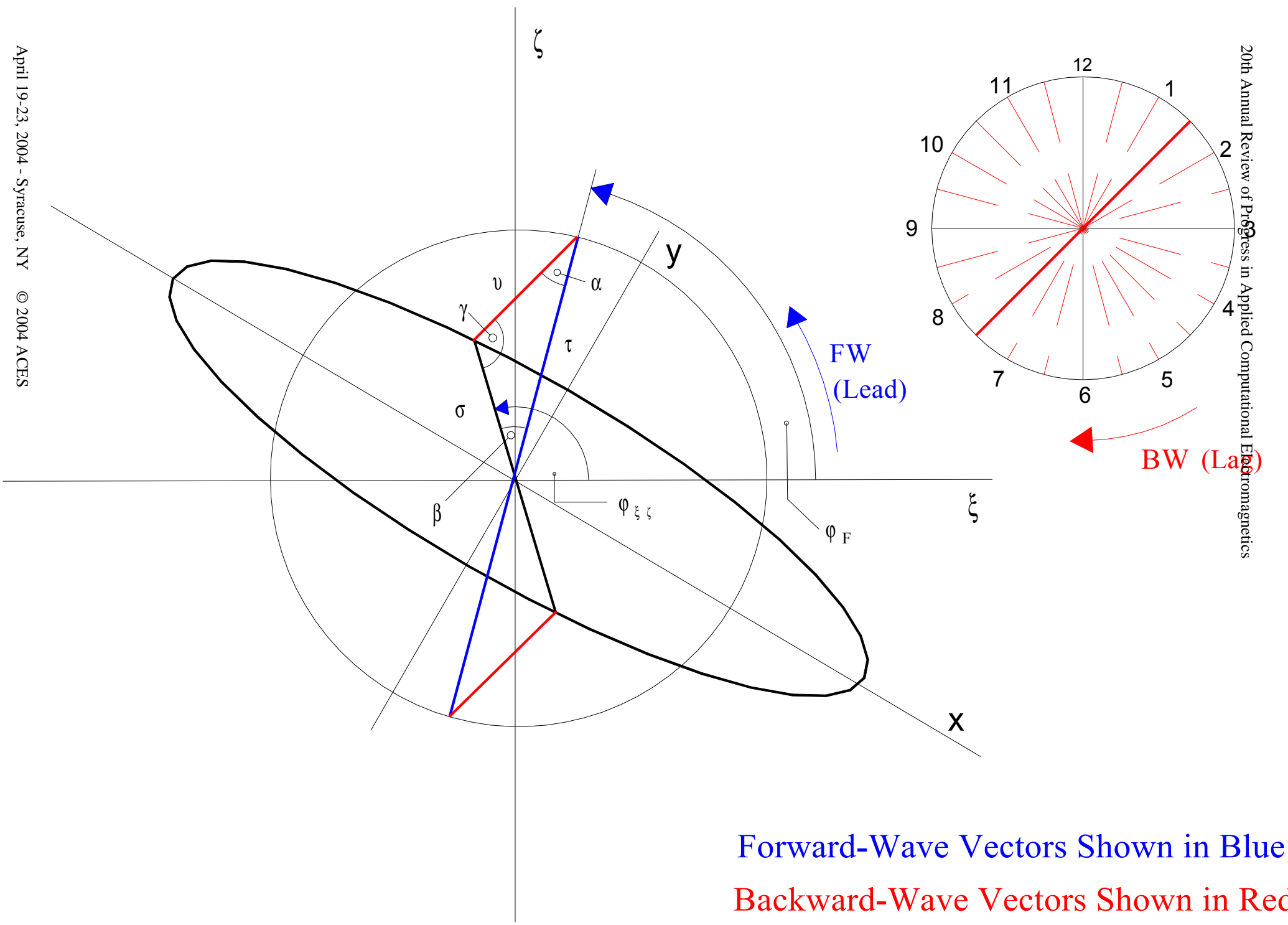
**Figure 3 - The Tilted-Ellipse Representation of a Standing-Wave Pattern.**



Forward-Wave Vectors Shown in Blue  
Backward-Wave Vectors Shown in Red

Figure 4 - The Tilted-Ellipse Representation of a Standing-Wave Pattern.





Forward-Wave Vectors Shown in Blue  
 Backward-Wave Vectors Shown in Red

Figure 5 - The Tilted-Ellipse Representation of a Standing-Wave Pattern.

Figure 6 - Detail of the Vector-Addition Triangle.

Forward-Wave Vector Shown in Blue.

Backward-Wave Vector Shown in Red.

Vector-Addition in the First Quadrant.

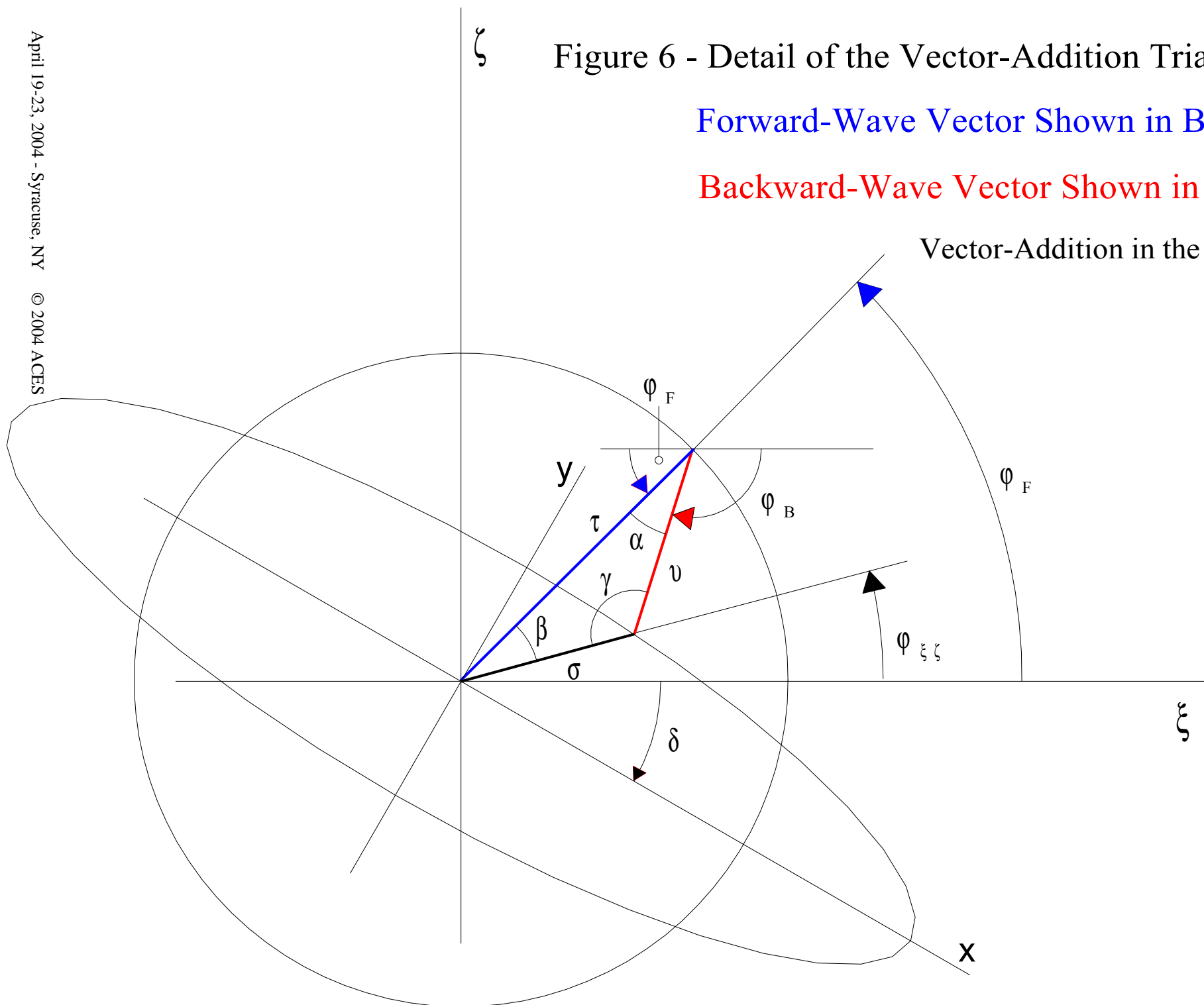
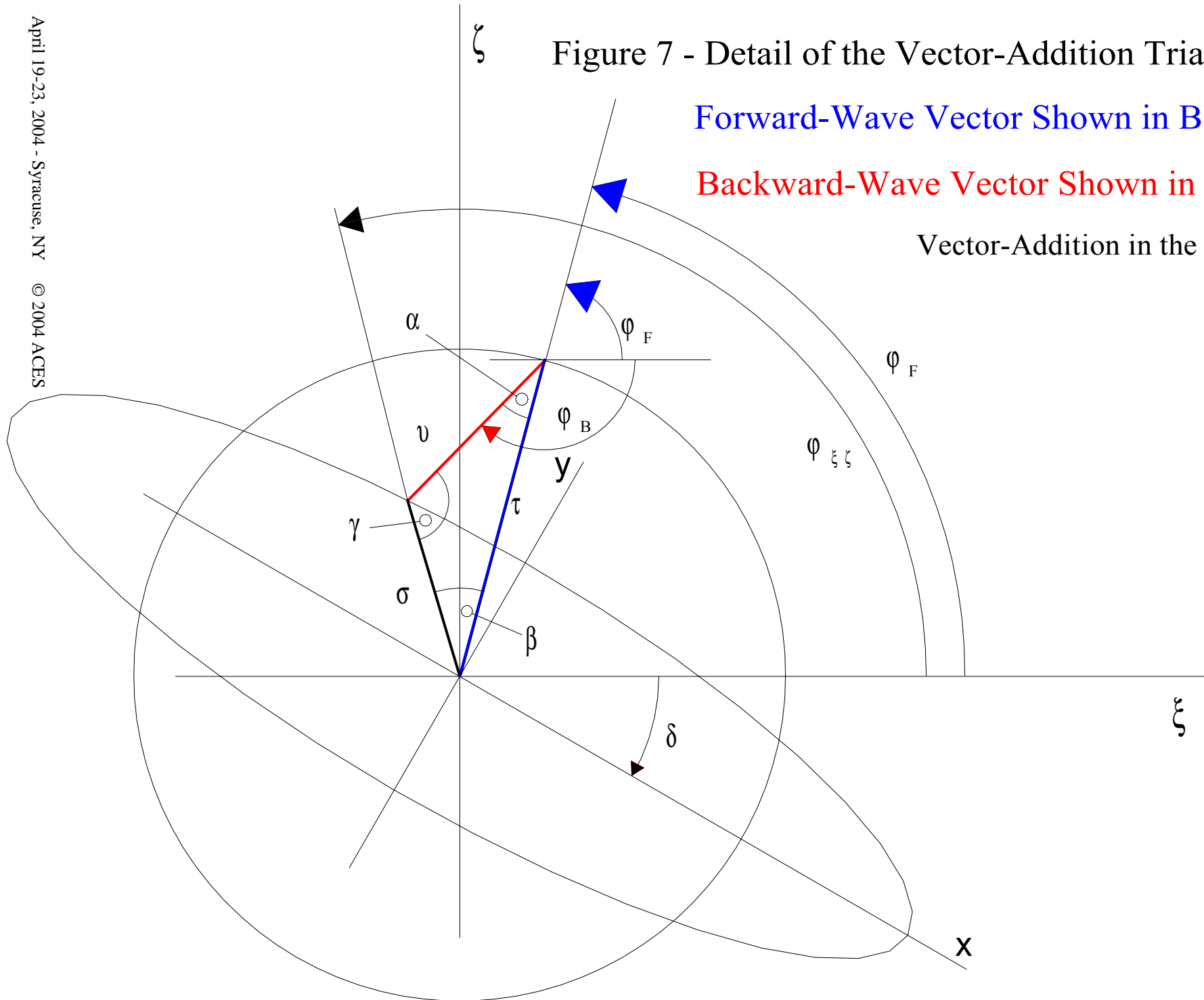


Figure 7 - Detail of the Vector-Addition Triangle.

Forward-Wave Vector Shown in Blue.

Backward-Wave Vector Shown in Red.

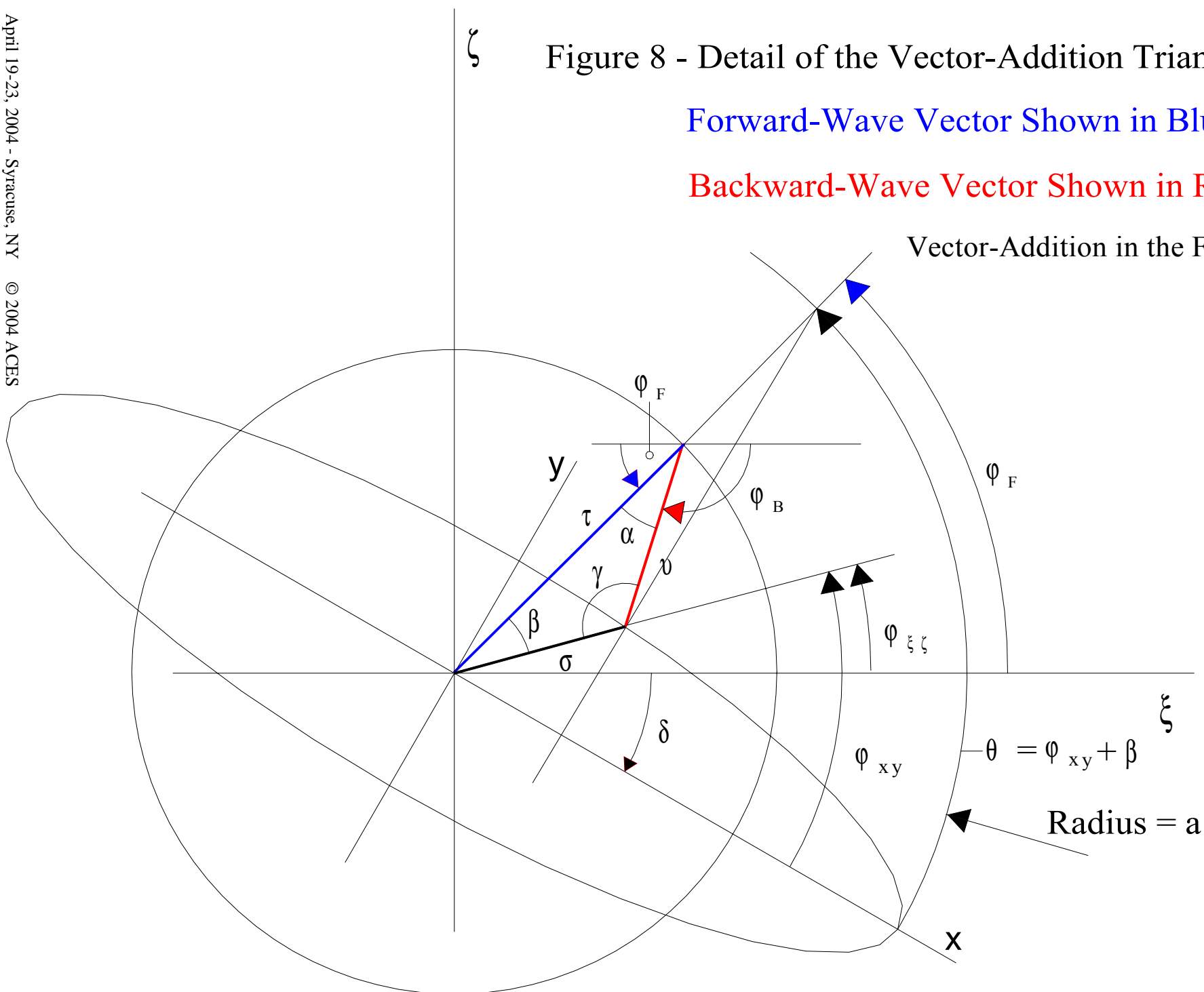
Vector-Addition in the Second Quadrant.



Forward-Wave Vector Shown in Blue.

Backward-Wave Vector Shown in Red.

## Vector-Addition in the First Quadrant.



Radius = a

$$\theta = \varphi_{xy} + \beta$$

# APPENDIX - 2

Graphic Displays of the Inner-Angles  $\alpha$  ,  $\beta$  ,  $\gamma$  ,  
and of the Phase-Angles  $\varphi_F$  ,  $\varphi_B$  , and  $\varphi_\Gamma$  .

(NOTE: All Graphic Displays are Generated Assuming:  $\rho = 1/4$  , and  $\delta = 30^\circ$  ).



## Figure Captions.

- FIGURE 1 - SINES OF THE INNER-ANGLES  $\alpha$  (SOLID),  $\beta$  (DASHED), AND  $\gamma$  (DASH-DOT).
- FIGURE 2 - COSINES OF THE INNER-ANGLES  $\alpha$  (SOLID),  $\beta$  (DASHED), AND  $\gamma$  (DASH-DOT).
- FIGURE 3 - TANGENTS OF THE INNER-ANGLES  $\alpha$  (SOLID),  $\beta$  (DASHED), AND  $\gamma$  (DASH-DOT).
- FIGURE 4 - ANGLE  $\alpha$ :  $\alpha_1 = \text{asin}(\sin \alpha)$  (SOLID),  $\alpha_2 = \text{acos}(\cos \alpha)$  (DASHED),  $\alpha_3 = \text{atan}(\tan \alpha)$  (DASH-DOT).
- FIGURE 5 - ANGLE  $\beta$ :  $\beta_1 = \text{asin}(\sin \beta)$  (SOLID),  $\beta_2 = \text{acos}(\cos \beta)$  (DASHED),  $\beta_3 = \text{atan}(\tan \beta)$  (DASH-DOT).
- FIGURE 6 - ANGLE  $\gamma$ :  $\gamma_1 = \text{asin}(\sin \gamma)$  (SOLID),  $\gamma_2 = \text{acos}(\cos \gamma)$  (DASHED),  $\gamma_3 = \text{atan}(\tan \gamma)$  (DASH-DOT).
- FIGURE 7 - INNER-ANGLES  $\alpha$  ( $\alpha_2$  SOLID),  $\beta$  ( $\beta_2$  DASHED), AND  $\gamma$  ( $\gamma_2$  DASH-DOT).
- FIGURE 8 - SINES OF THE ANGLES  $\phi_{xy}$  (SOLID) AND  $\theta$  (DASHED).
- FIGURE 9 - COSINES OF THE ANGLES  $\phi_{xy}$  (SOLID) AND  $\theta$  (DASHED).
- FIGURE 10 - TangentS OF THE ANGLES  $\phi_{xy}$  (SOLID) AND  $\theta$  (DASHED).
- FIGURE 11 - ANGLES  $\phi_{xy1} = \text{asin}(\sin \phi_{xy})$  (SOLID),  $\phi_{xy2} = \text{acos}(\cos \phi_{xy})$  (DASHED),  $\phi_{xy3} = \text{atan}(\tan \phi_{xy})$  (DASH-DOT).
- FIGURE 12 - SINES OF THE ANGLES  $\phi_{Fxy1}$  (SOLID) AND  $\theta$  (DASHED).
- FIGURE 13 - COSINES OF THE ANGLES  $\phi_{Fxy1}$  (SOLID) AND  $\theta$  (DASHED).
- FIGURE 14 - TANGENTS OF THE ANGLES  $\phi_{Fxy1}$  (SOLID) AND  $\theta$  (DASHED).
- FIGURE 15 - SINES OF THE ANGLES  $\phi_{Fxy2}$  (SOLID) AND  $\theta$  (DASHED).
- FIGURE 16 - COSINES OF THE ANGLES  $\phi_{Fxy2}$  (SOLID) AND  $\theta$  (DASHED).
- FIGURE 17 - TANGENTS OF THE ANGLES  $\phi_{Fxy2}$  (SOLID) AND  $\theta$  (DASHED).
- FIGURE 18 -  $\phi_{Fxy1a} = \text{asin}(\sin \phi_{Fxy1})$  (SOLID),  $\phi_{Fxy1b} = \text{acos}(\cos \phi_{Fxy1})$  (DASHED),  $\phi_{Fxy1c} = \text{atan}(\tan \phi_{Fxy1})$  ( DASH-DOT).
- FIGURE 19 -  $\phi_{Fxy2a} = \text{asin}(\sin \phi_{Fxy2})$  (SOLID),  $\phi_{Fxy2b} = \text{acos}(\cos \phi_{Fxy2})$  (DASHED),  $\phi_{Fxy2c} = \text{atan}(\tan \phi_{Fxy2})$  ( DASH-DOT).
- FIGURE 20 -  $\phi_{Fxy1a} = \text{asin}(\sin \phi_{Fxy1})$  (SOLID),  $\beta_1 = \text{asin}(\sin \beta)$  (DASHED),  $\phi_{xy1} = \text{asin}(\sin \phi_{xy})$  ( DASH-DOT).

NOTE: All Graphic Displays are Generated Assuming:  $\rho = 1/4$  , and  $\delta = 30^\circ$  .

FIGURE 1 – SINES OF THE INNER-ANGLES Alpha (SOLID), Beta (DASHED), AND Gamma (DASH-DOT)

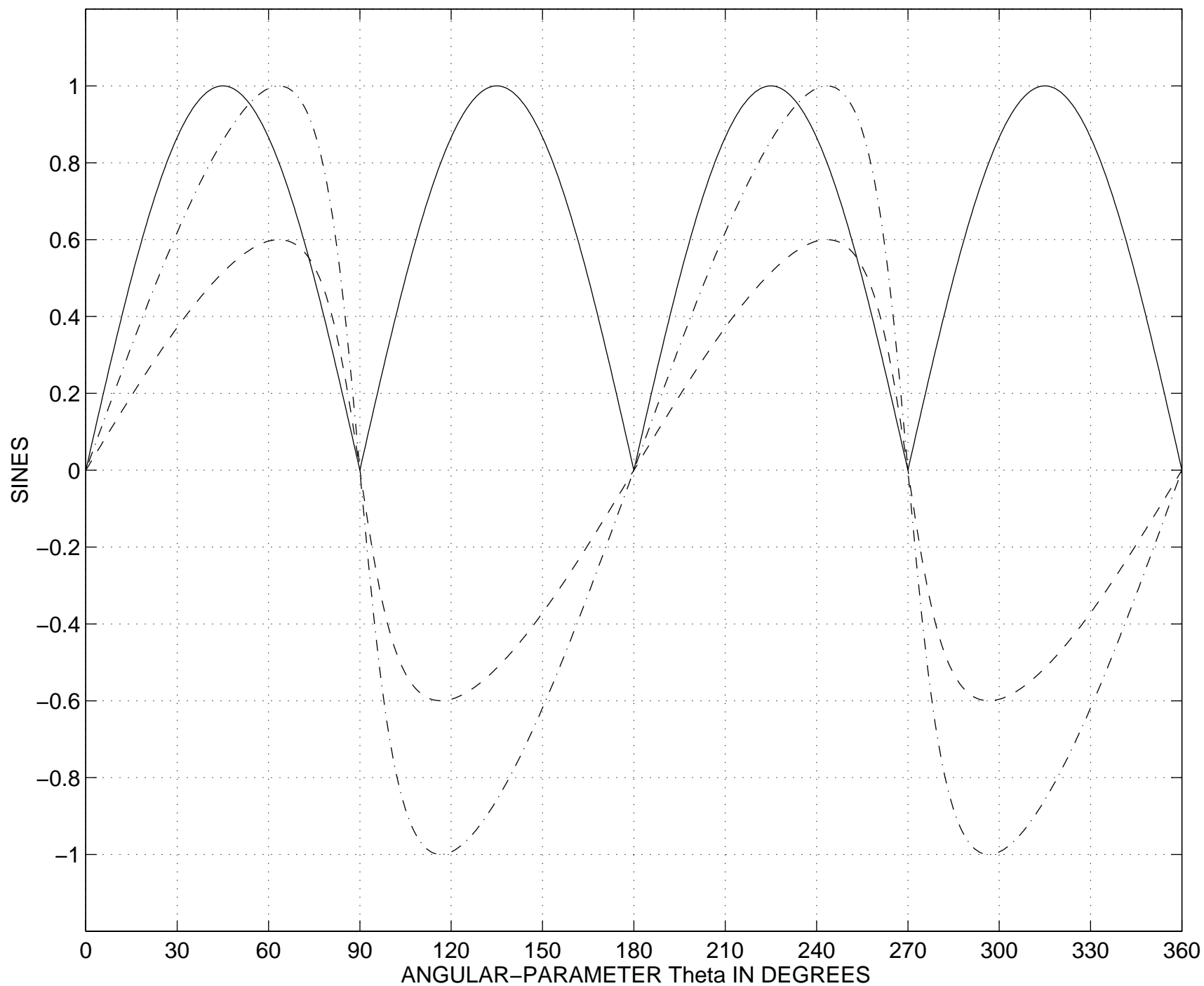


FIGURE 2 – COSINES OF THE INNER-ANGLES Alpha (SOLID), Beta (DASHED), AND Gamma (DASH-DOT)

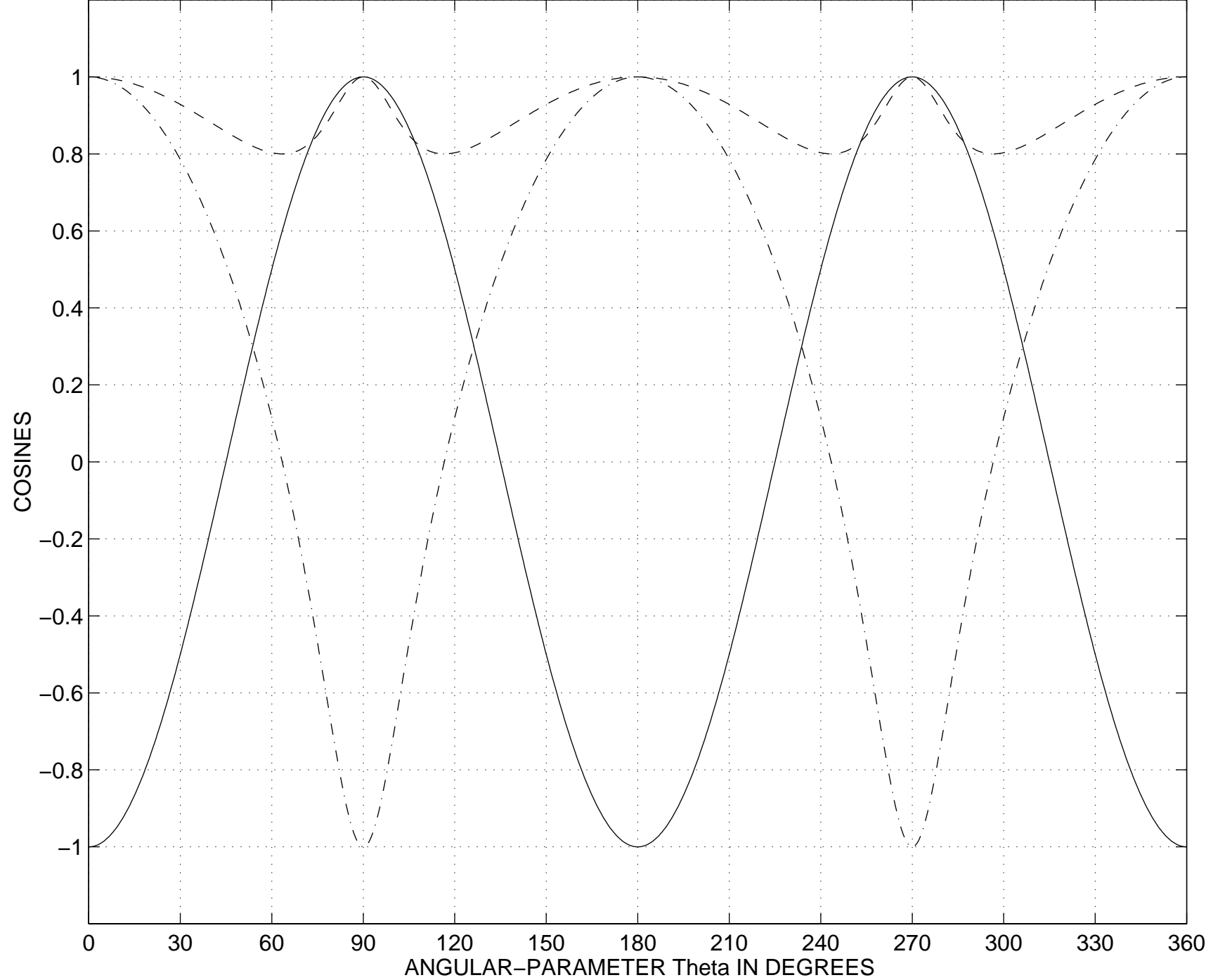
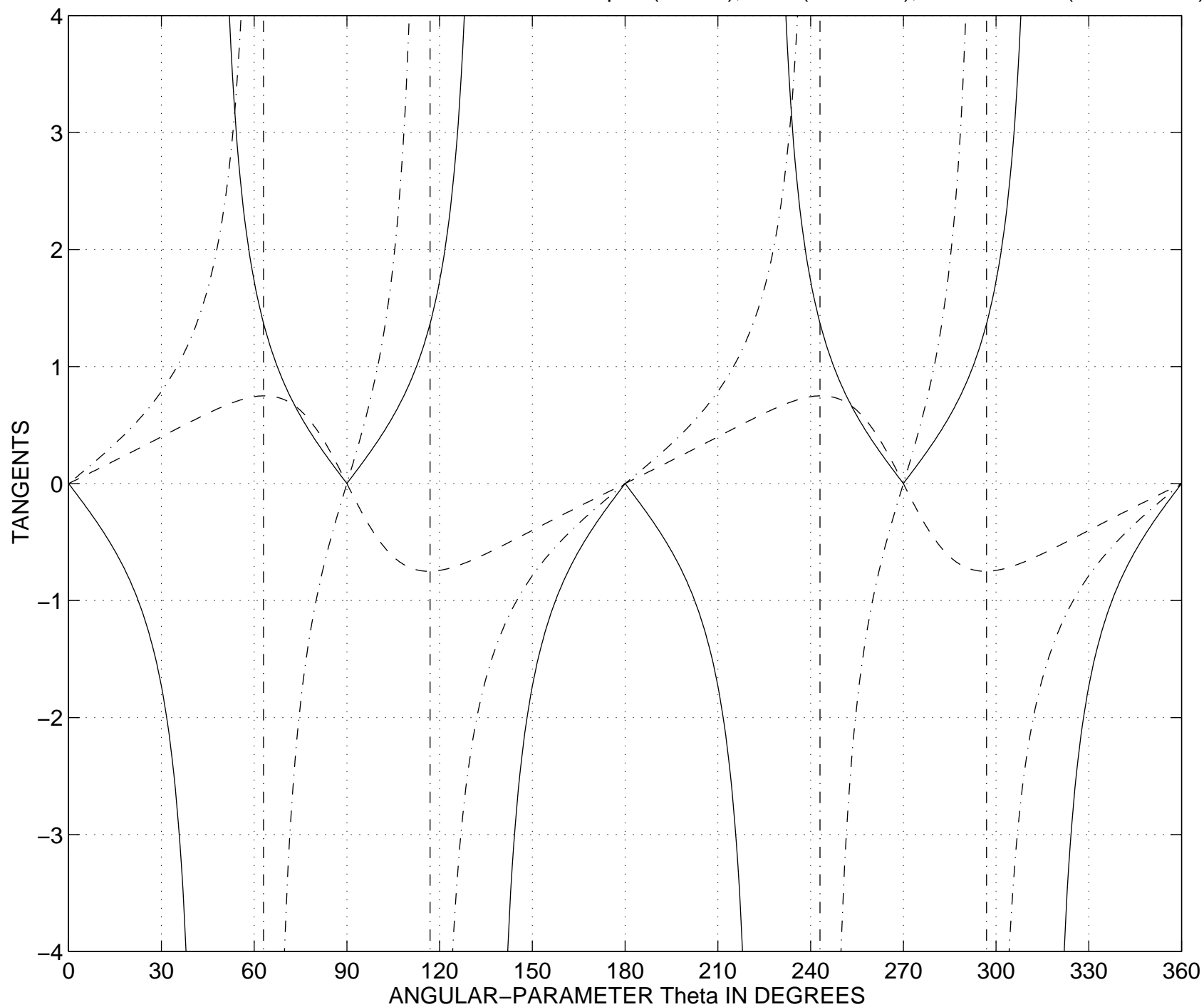
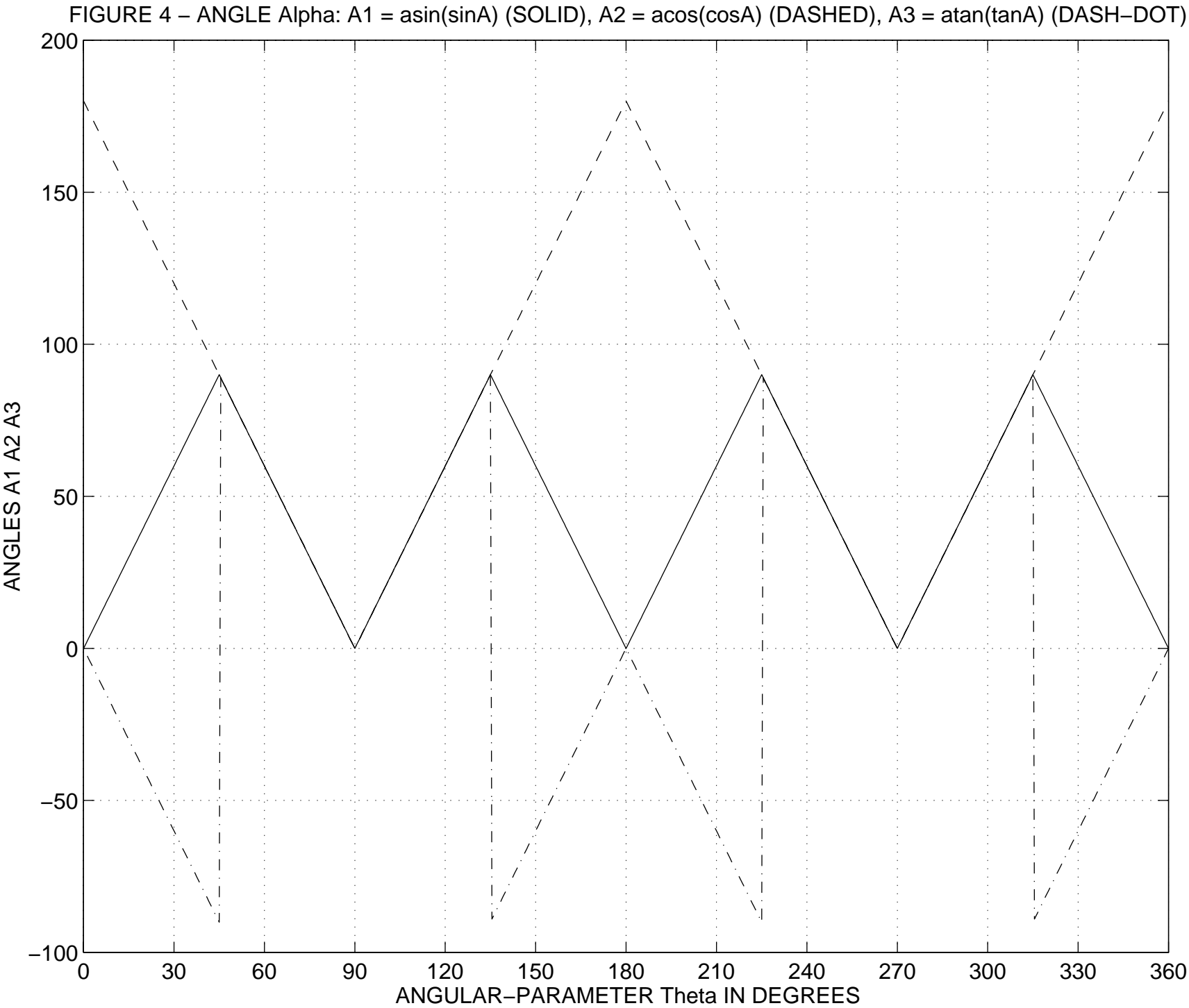




FIGURE 3 – TANGENTS OF THE INNER-ANGLES Alpha (SOLID), Beta (DASHED), AND Gamma (DASH-DOT)





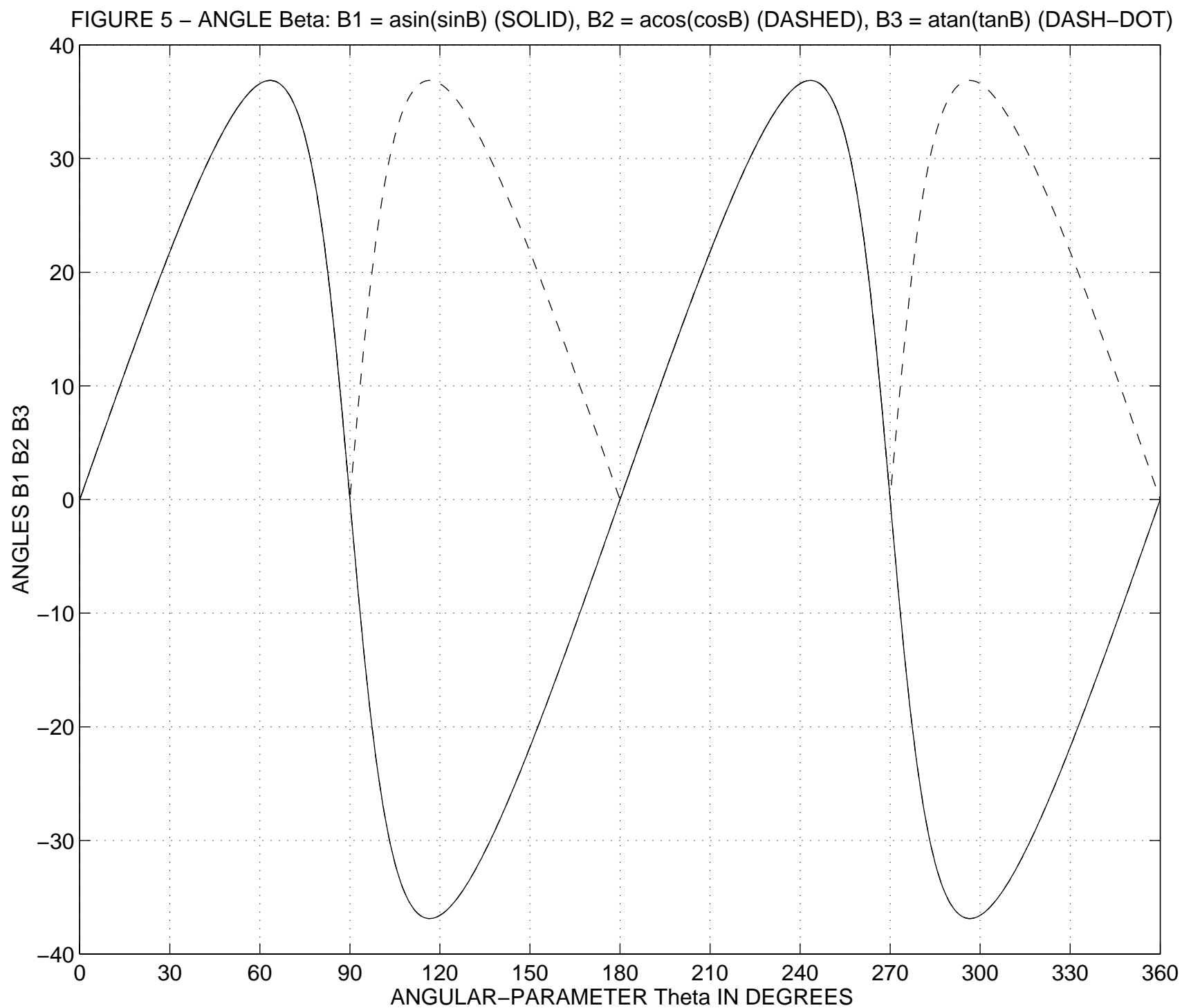
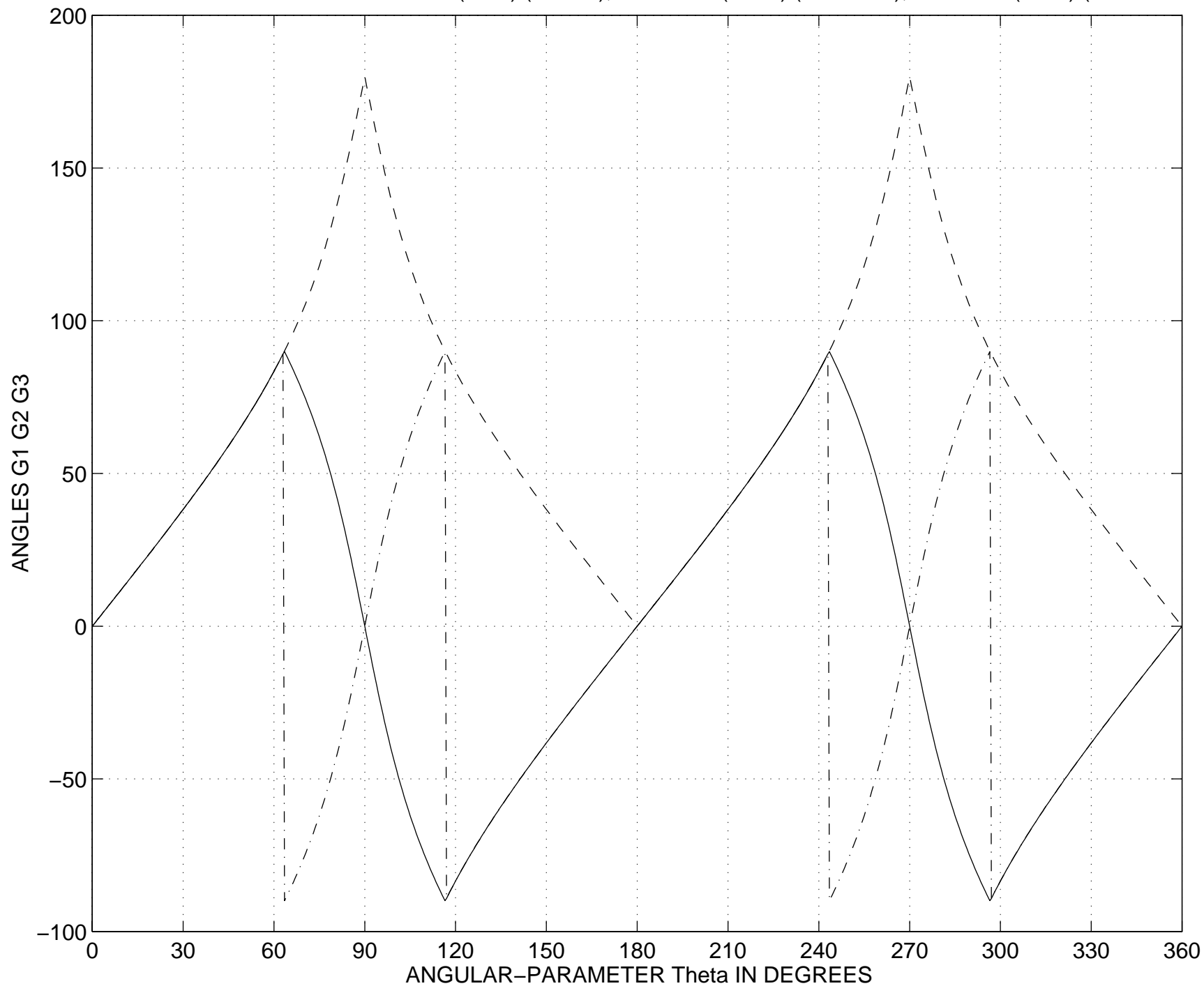


FIGURE 6 – ANGLE Gamma: G1 =  $\text{asin}(\sin G)$  (SOLID), G2 =  $\text{acos}(\cos G)$  (DASHED), G3 =  $\text{atan}(\tan G)$  (DASH-DOT)



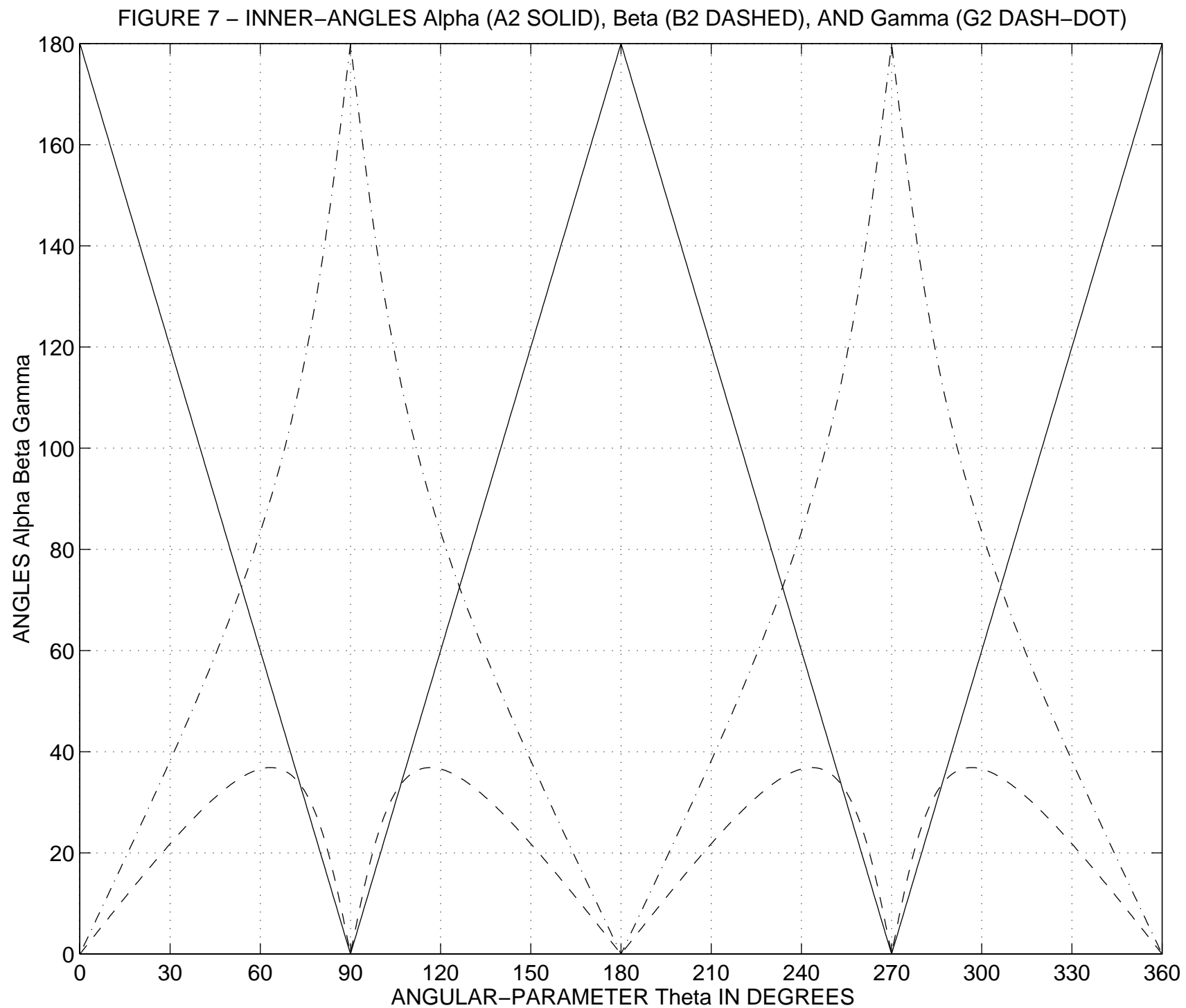


FIGURE 8 – SINES OF THE ANGLES Phixy (SOLID) AND Theta (DASHED)

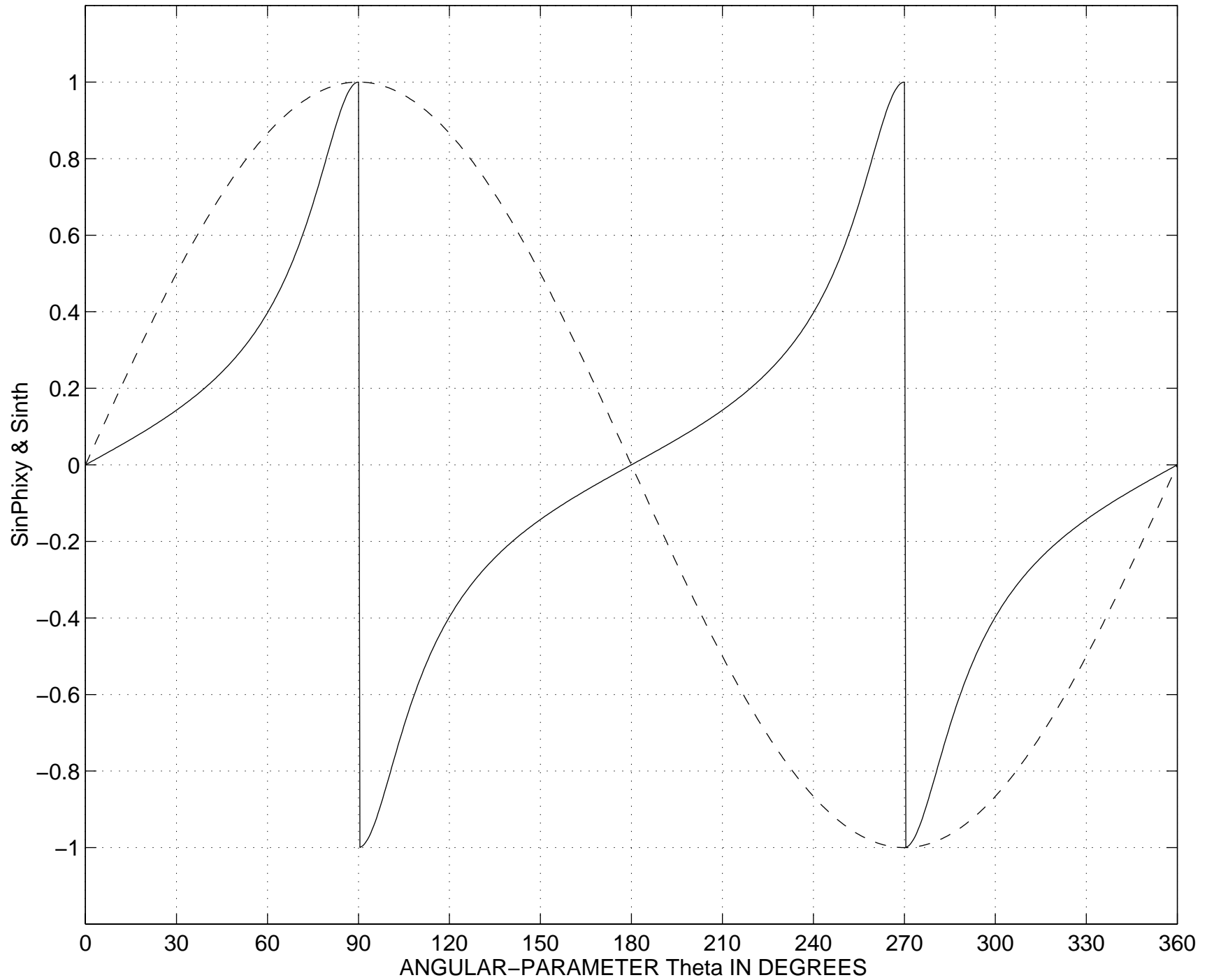


FIGURE 9 – COSINES OF THE ANGLES Phixy (SOLID) AND Theta (DASHED)

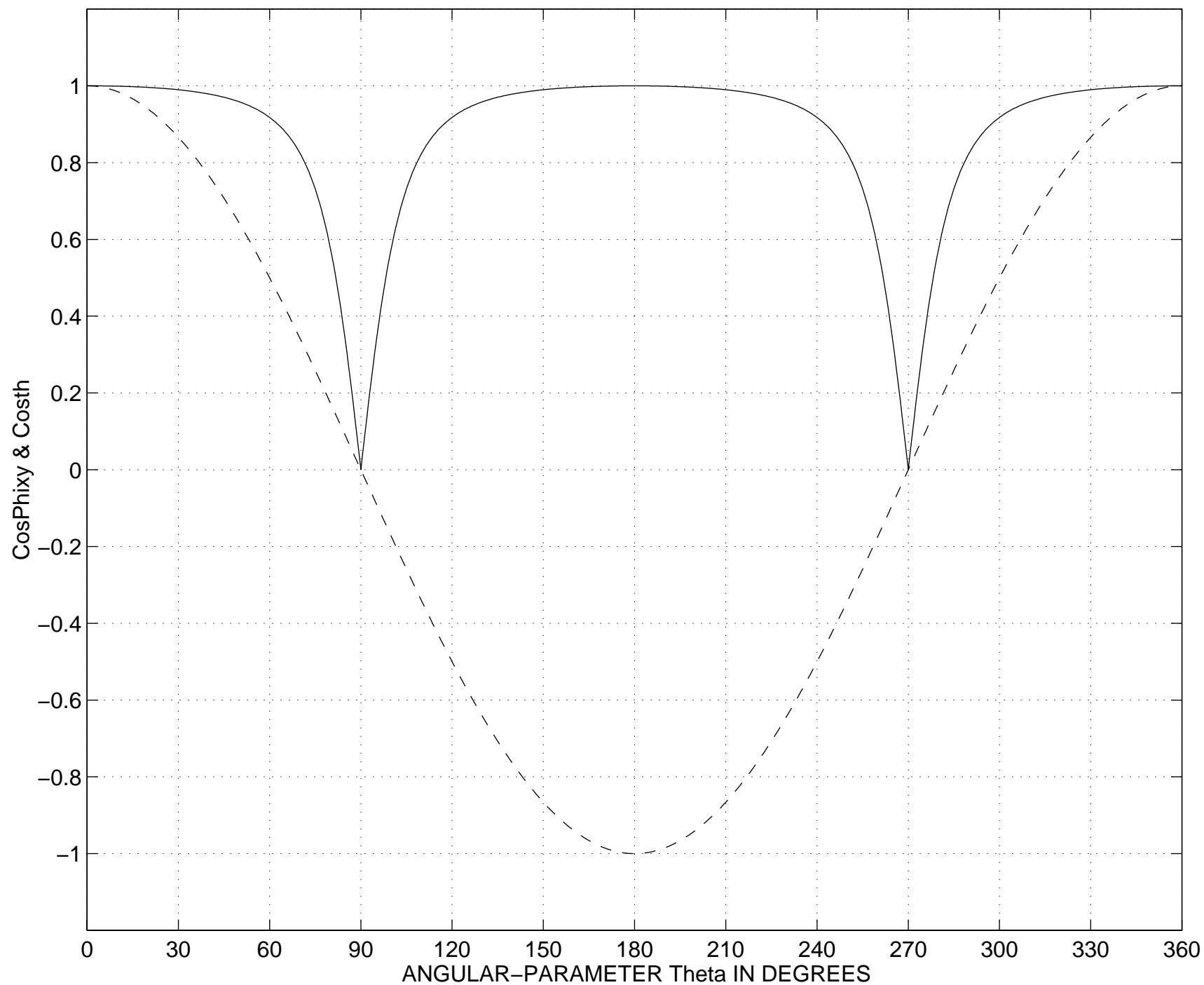


FIGURE 10 – Tangents OF THE ANGLES Phixy (SOLID) AND Theta (DASHED)

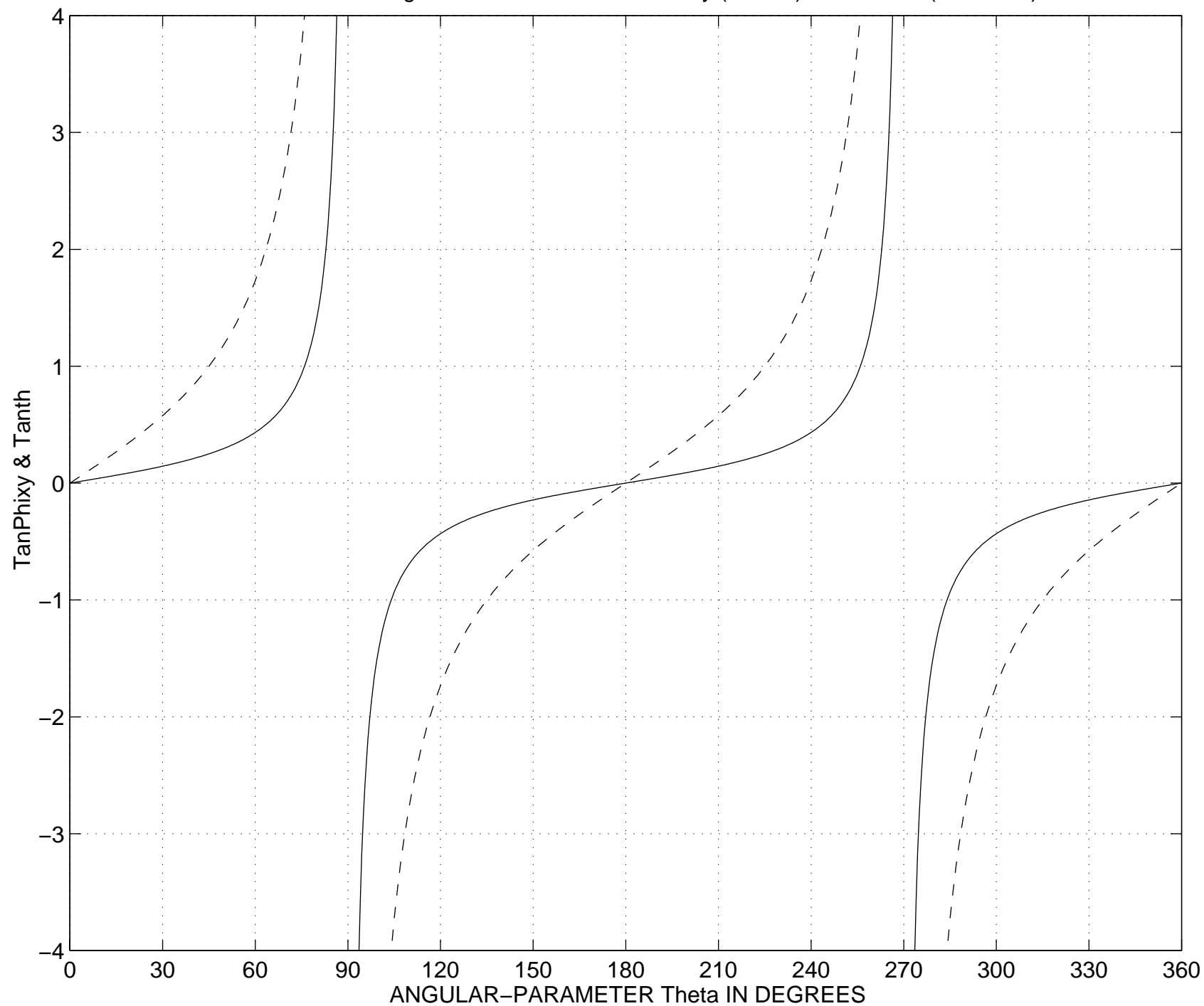




FIGURE 11 – Phixy1 = asin(SinPhixy) (SOLID), Phixy2 = acos(CosPhixy) (DASHED), Phixy3 = atan(TanPhixy) (DASH-DOT)

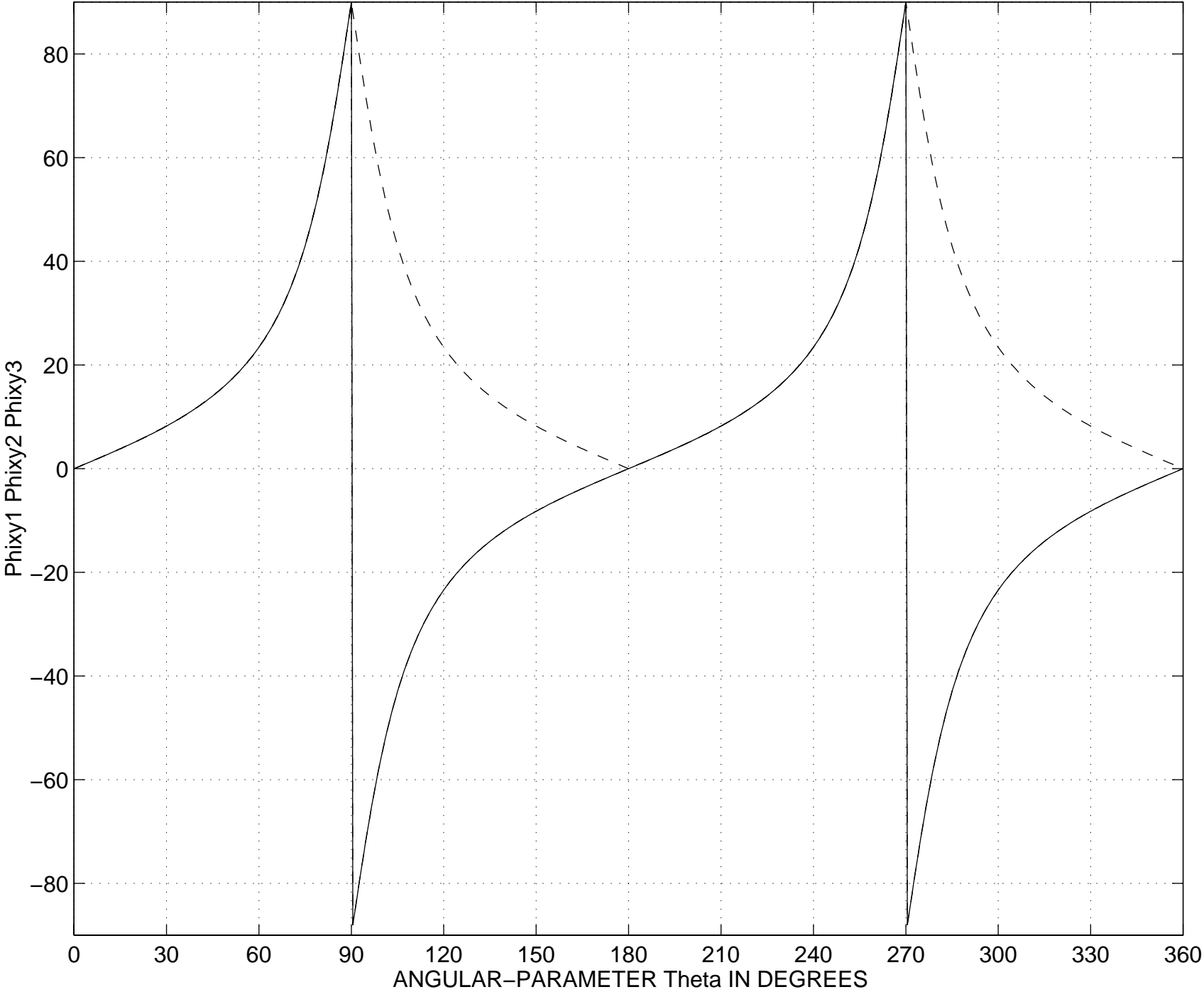


FIGURE 12 – SINES OF THE ANGLES  $\Phi_1$  (SOLID) AND  $\Theta$  (DASHED)

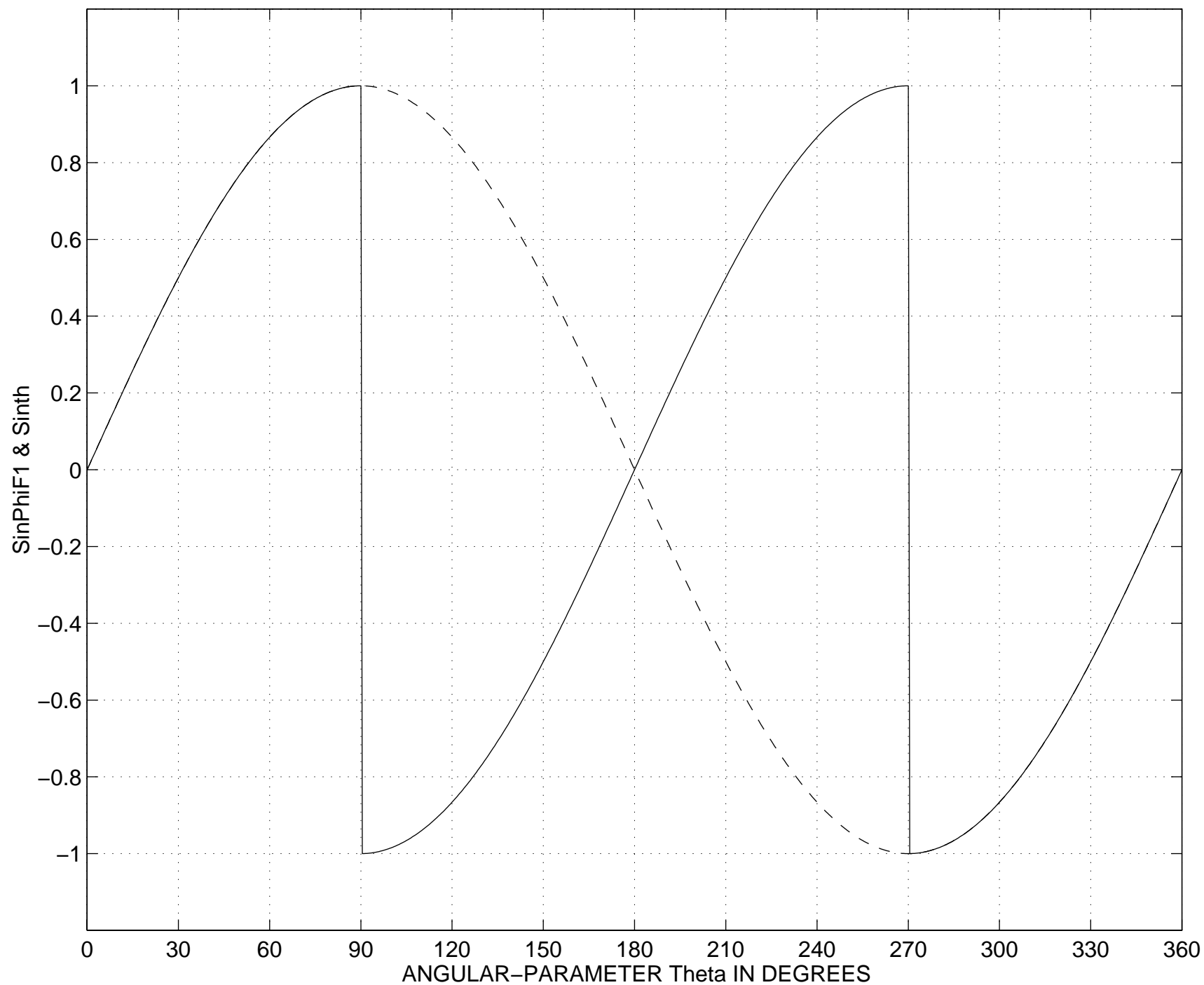
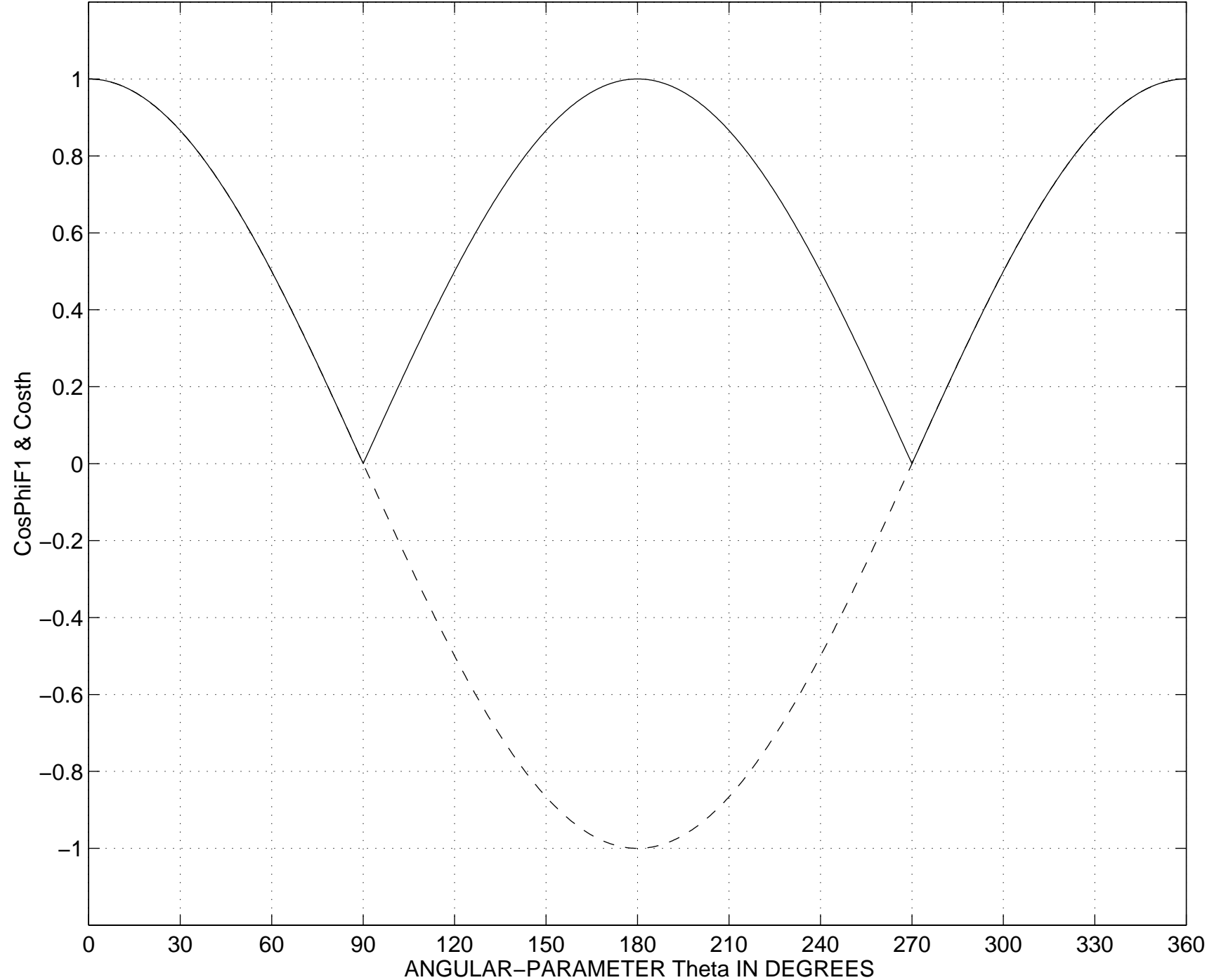


FIGURE 13 – COSINES OF THE ANGLES PhiF1 (SOLID) AND Theta (DASHED)



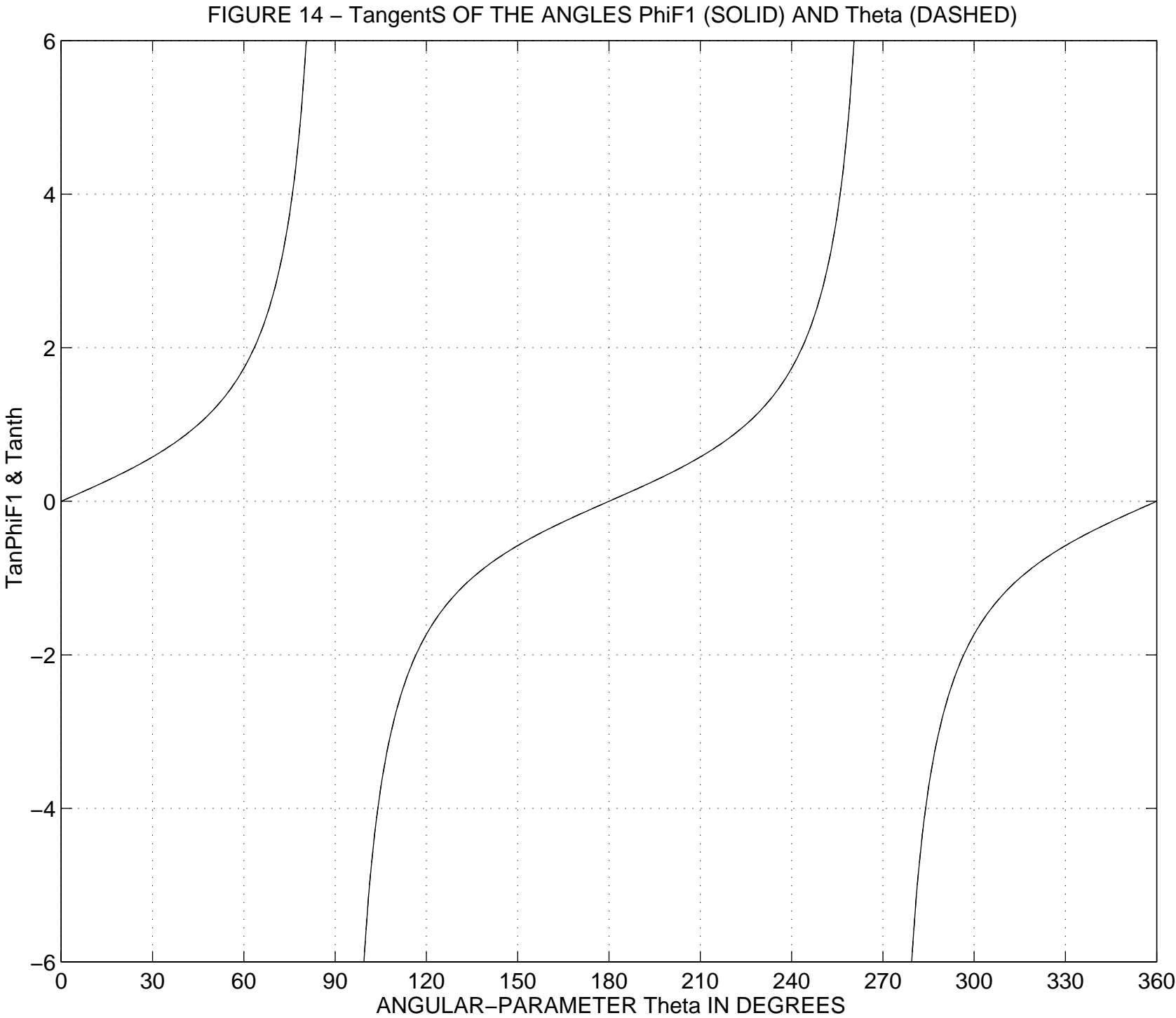


FIGURE 15 – SINES OF THE ANGLES PhiF2 (SOLID) AND Theta (DASHED)

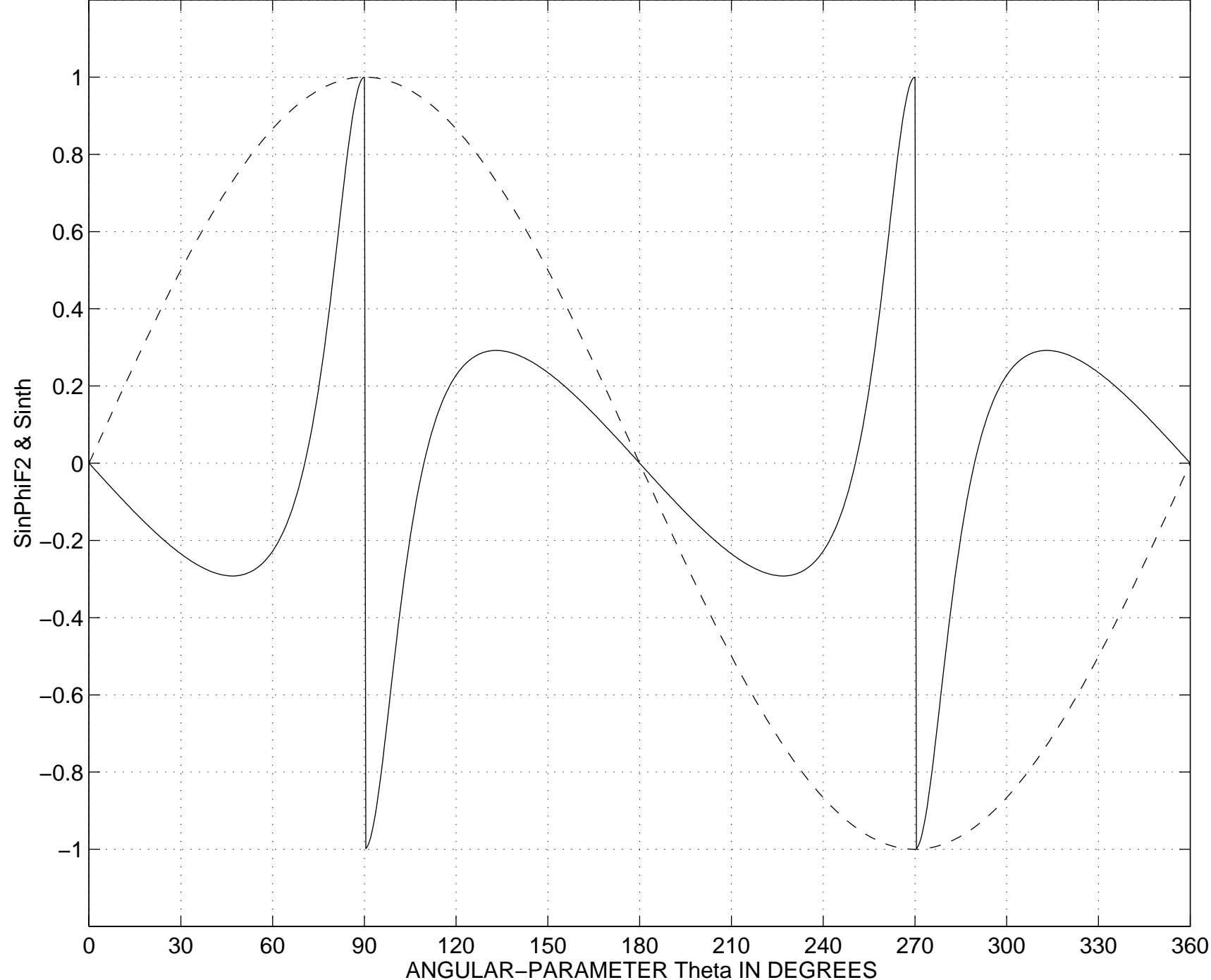
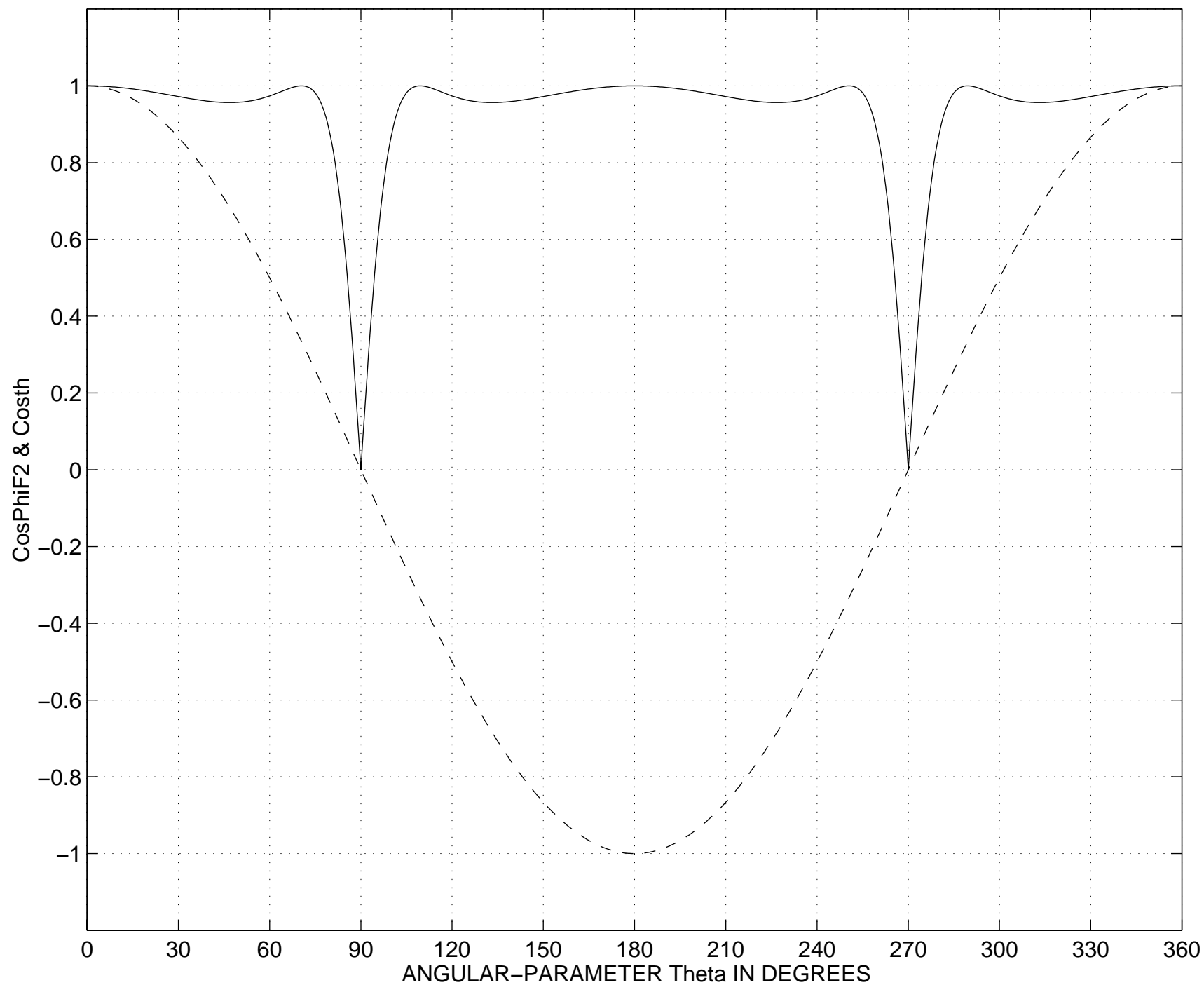


FIGURE 16 – COSINES OF THE ANGLES PhiF2 (SOLID) AND Theta (DASHED)



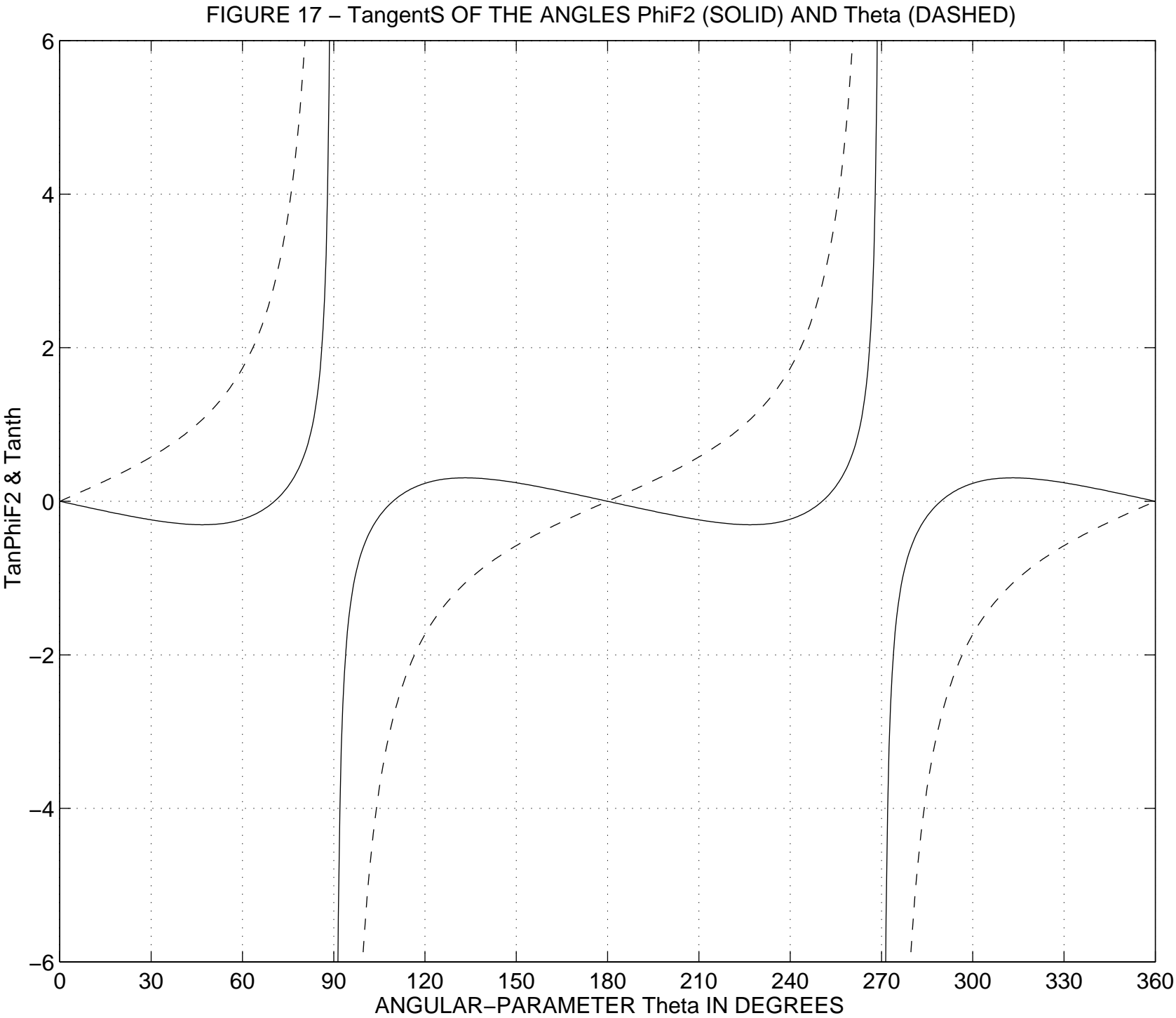


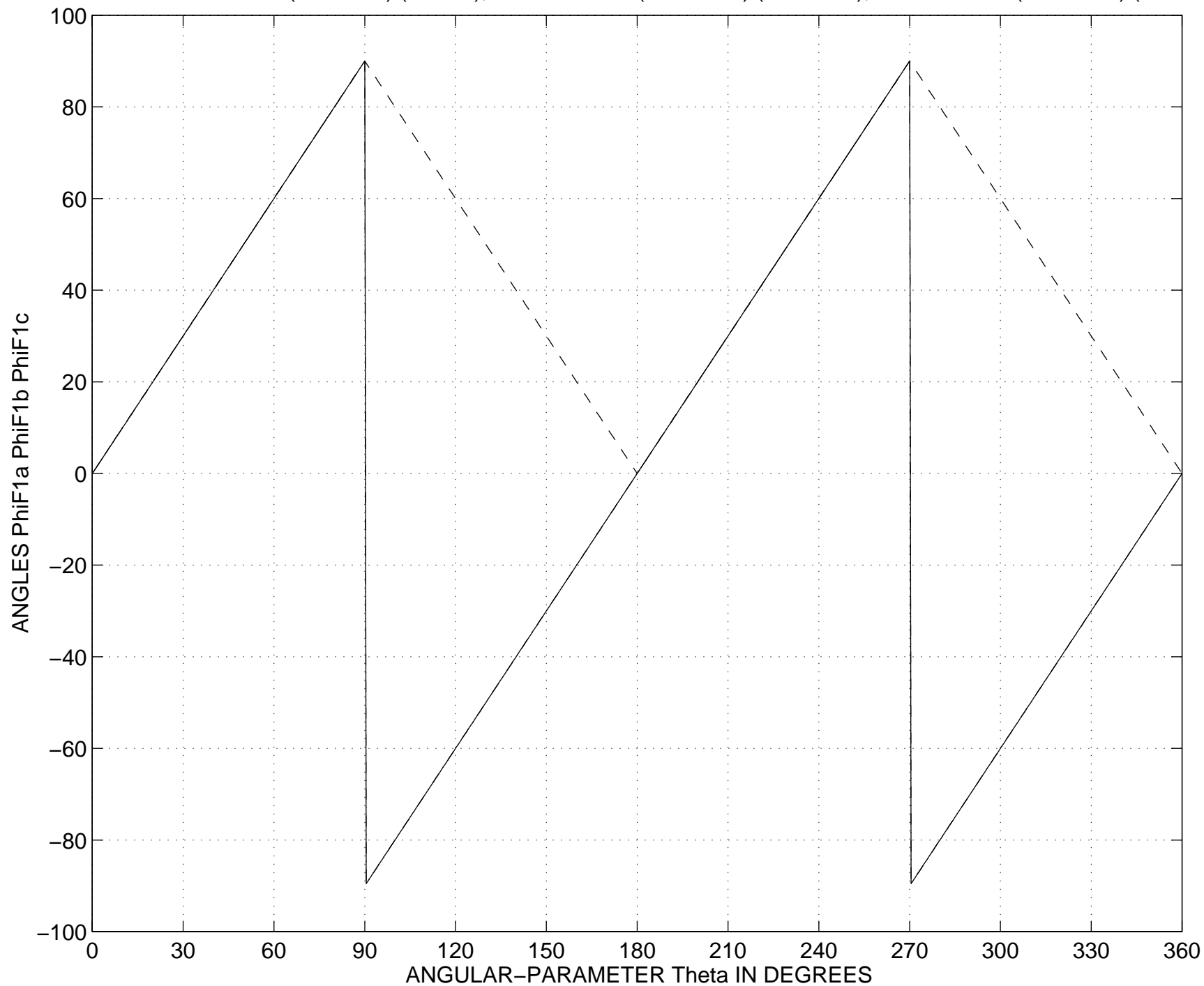
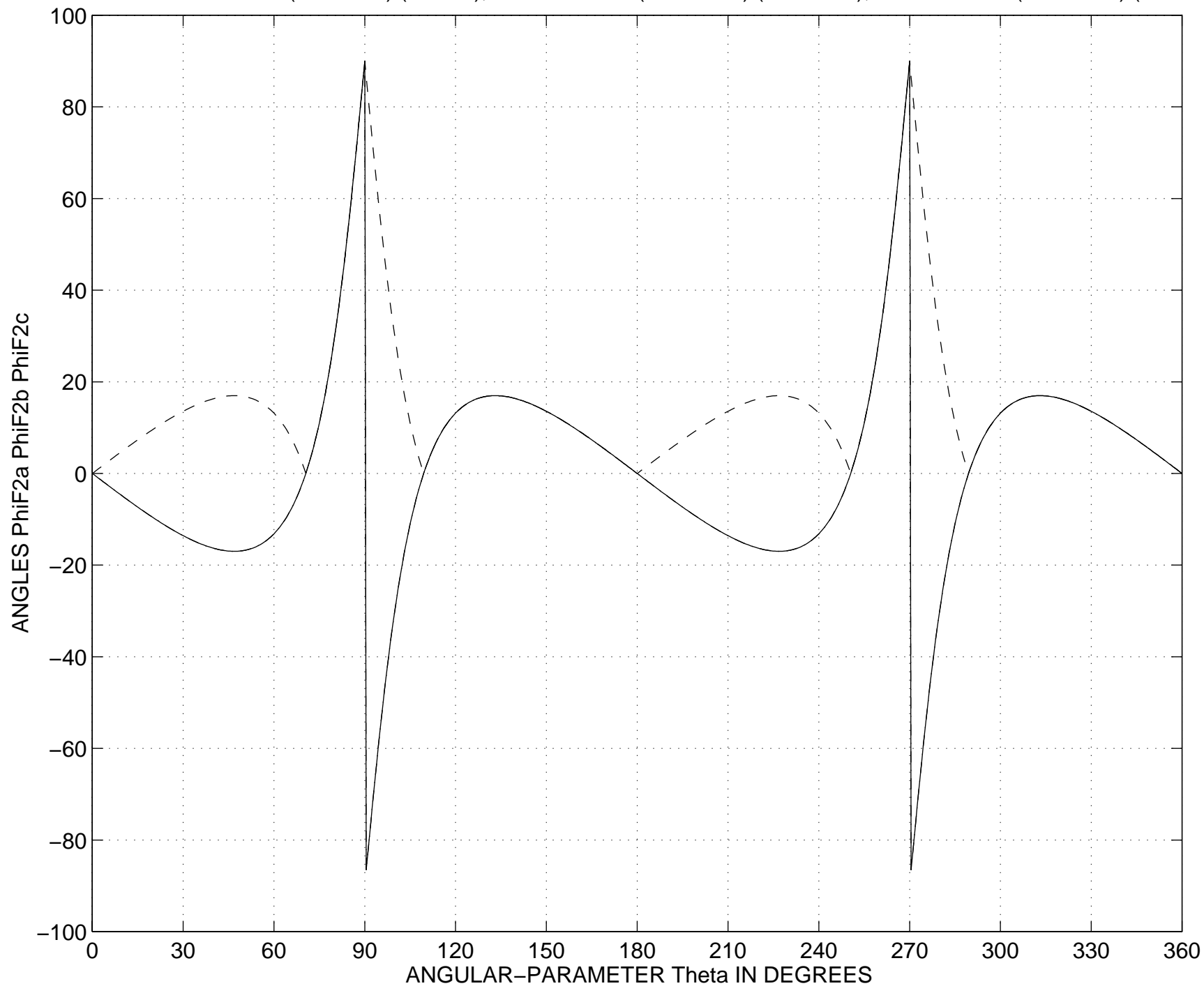
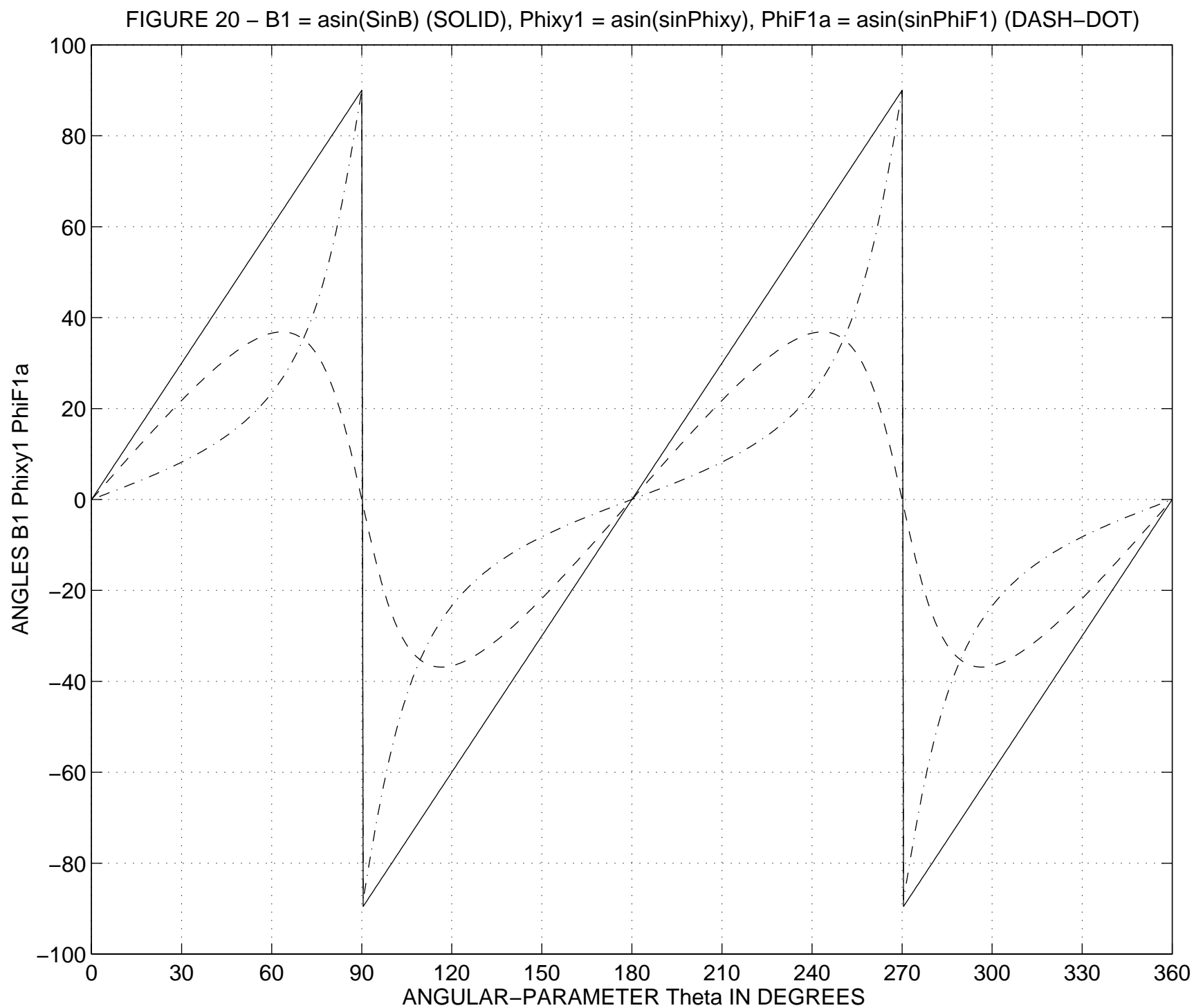
FIGURE 18 –  $\Phi_{1a} = \arcsin(\sin\Phi_1)$  (SOLID),  $\Phi_{1b} = \arccos(\cos\Phi_1)$  (DASHED),  $\Phi_{1c} = \arctan(\tan\Phi_1)$  (DASH-DOT)



FIGURE 19 –  $\Phi_{F2a} = \arcsin(\sin \Phi_{F2})$  (SOLID),  $\Phi_{F2b} = \arccos(\cos \Phi_{F2})$  (DASHED),  $\Phi_{F2c} = \arctan(\tan \Phi_{F2})$  (DASH-DOT)



# APPENDIX - 3

## Closed-Form Expressions of the Trigonometric Functions of the Phase-Angles $\varphi_{F1}$ and $\varphi_{F2}$ .

*( Using the Expressions of the Vector-Addition Triangle Inner-Angles  $\alpha$ ,  $\beta$ , and  $\gamma$  ).*



## Closed-Form Expressions of the Trigonometric Functions of the Phase-Angles $\Phi_{F1}$ and $\Phi_{F2}$ .

Expressions of the Tangents of the angles  $\Phi_{xy}$  and  $\beta$  :

$$\tan \Phi_{xy} = \frac{y}{x} = \frac{b \sin \theta}{a \cos \theta} = \rho \tan \theta \quad (1)$$

$$\tan \beta = \frac{(1-\rho) \sin \theta \cos \theta}{1-(1-\rho) \sin^2 \theta} \quad (2)$$

Expressions of the Tangent of the Phase-Angles  $\Phi_{F1}$ :

$$\begin{aligned} \tan \Phi_{F1} &= \tan(\Phi_{xy} + \beta) = \frac{\tan \Phi_{xy} + \tan \beta}{1 - \tan \Phi_{xy} \tan \beta} = \frac{\rho \tan \theta + \frac{(1-\rho) \sin \theta \cos \theta}{1-(1-\rho) \sin^2 \theta}}{1 - \rho \tan \theta \frac{(1-\rho) \sin \theta \cos \theta}{1-(1-\rho) \sin^2 \theta}} = \\ &= \frac{\rho \tan \theta [1-(1-\rho) \sin^2 \theta] + (1-\rho) \tan \theta \cos^2 \theta}{[1-(1-\rho) \sin^2 \theta] - \rho \tan \theta (1-\rho) \tan \theta \cos^2 \theta} = \tan \theta \frac{\rho [1-(1-\rho) \sin^2 \theta] + (1-\rho) (1 - \sin^2 \theta)}{[1-(1-\rho) \sin^2 \theta] - \rho (1-\rho) \sin^2 \theta} \quad (3) \\ &= \tan \theta \frac{\rho + (1-\rho) - \rho (1-\rho) \sin^2 \theta - (1-\rho) \sin^2 \theta}{1-(1-\rho) \sin^2 \theta - \rho (1-\rho) \sin^2 \theta} = \tan \theta \frac{1 - (1-\rho^2) \sin^2 \theta}{1 - (1-\rho^2) \sin^2 \theta} = \tan \theta \end{aligned}$$

## Closed-Form Expressions of the Trigonometric Functions of the Phase-Angles $\Phi_{F1}$ and $\Phi_{F2}$ .

Substitution of the expression of the Aspect-Ratio  $\rho$  as Function of the Tangent of the angle  $\Phi_{xy}$  in the Tangent of  $\beta$  :

$$\rho = \frac{\tan \Phi_{xy}}{\tan \theta} \quad (1^a) \quad \tan \beta = \frac{\left(1 - \frac{\tan \Phi_{xy}}{\tan \theta}\right) \sin \theta \cos \theta}{1 - \left(1 - \frac{\tan \Phi_{xy}}{\tan \theta}\right) \sin^2 \theta} \quad (2^a)$$

Simplification of the Expressions of the Tangent of the Tangent of  $\beta$  :

$$\begin{aligned} \tan \beta &= \frac{\left(1 - \frac{\tan \Phi_{xy}}{\tan \theta}\right) \sin \theta \cos \theta}{1 - \left(1 - \frac{\tan \Phi_{xy}}{\tan \theta}\right) \sin^2 \theta} = \frac{(\tan \theta - \tan \Phi_{xy}) \tan \theta \cos^2 \theta}{\tan \theta - (\tan \theta - \tan \Phi_{xy}) \sin^2 \theta} = \frac{(\tan \theta - \tan \Phi_{xy}) \tan \theta (1 - \sin^2 \theta)}{\tan \theta - (\tan \theta - \tan \Phi_{xy}) \sin^2 \theta} = \\ &= \frac{(\tan \theta - \tan \Phi_{xy}) \tan \theta \left(1 - \frac{\tan^2 \theta}{1 + \tan^2 \theta}\right)}{\tan \theta - (\tan \theta - \tan \Phi_{xy}) \left(\frac{\tan^2 \theta}{1 + \tan^2 \theta}\right)} = \tan \theta \frac{(\tan \theta - \tan \Phi_{xy}) (1 + \tan^2 \theta - \tan^2 \theta)}{\tan \theta (1 + \tan^2 \theta) - (\tan \theta - \tan \Phi_{xy}) \tan^2 \theta} = \\ &= \frac{\tan \theta - \tan \Phi_{xy}}{1 + \tan^2 \theta - \tan^2 \theta + \tan \theta \tan \Phi_{xy}} = \frac{\tan \theta - \tan \Phi_{xy}}{1 + \tan \theta \tan \Phi_{xy}} = \tan(\theta - \Phi_{xy}) \end{aligned} \quad (4)$$

# Closed-Form Expressions of the Trigonometric Functions of the Phase-Angles $\Phi_{F1}$ and $\Phi_{F2}$ .

Expressions of the Tangent of the Phase-Angles  $\Phi_{F2}$  :

$$\begin{aligned}
 \tan \Phi_{F2} &= \tan(\Phi_{xy} - \beta) = \frac{\tan \Phi_{xy} - \tan \beta}{1 + \tan \Phi_{xy} \tan \beta} = \frac{\rho \tan \theta - \frac{(1-\rho) \sin \theta \cos \theta}{1 - (1-\rho) \sin^2 \theta}}{1 + \rho \tan \theta \frac{(1-\rho) \sin \theta \cos \theta}{1 - (1-\rho) \sin^2 \theta}} = \\
 &= \frac{\rho \tan \theta [1 - (1-\rho) \sin^2 \theta] - (1-\rho) \tan \theta \cos^2 \theta}{[1 - (1-\rho) \sin^2 \theta] + \rho \tan \theta (1-\rho) \tan \theta \cos^2 \theta} = \tan \theta \frac{\rho - \rho(1-\rho) \sin^2 \theta - (1-\rho)(1 - \sin^2 \theta)}{1 - (1-\rho) \sin^2 \theta + \rho(1-\rho) \sin^2 \theta} = \\
 &= \tan \theta \frac{\rho - (1-\rho) - \rho(1-\rho) \sin^2 \theta + (1-\rho) \sin^2 \theta}{1 - (1-\rho) \sin^2 \theta (1-\rho)} = \tan \theta \frac{(2\rho - 1) - (1-\rho)^2 \sin^2 \theta}{1 - (1-\rho)^2 \sin^2 \theta} \neq \tan \theta
 \end{aligned}$$

